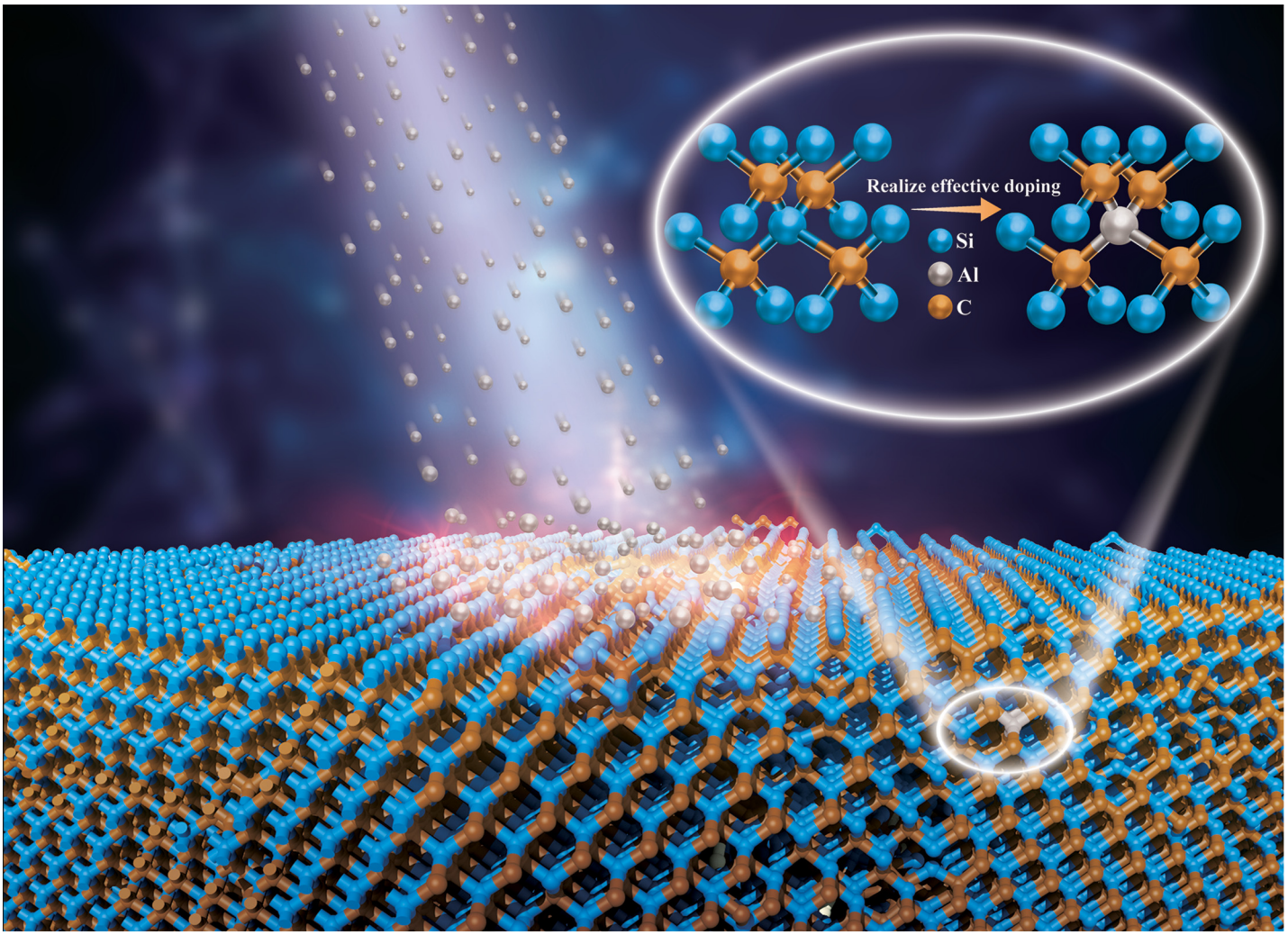


**Showcasing collaborative research from Tianjin University, China; Fraunhofer Institute for Integrated Systems and Device Technology IISB, Germany; Ruhr-University Bochum, Germany; University of Helsinki, Finland; and Southern University of Science and Technology, China.**

MD simulation study on defect evolution and doping efficiency of p-type doping of 3C-SiC by Al ion implantation with subsequent annealing.

Establishing an atomic-scale theoretical model for p-type doping by Al ion implantation will significantly contribute to improved understanding of defect formation mechanisms during ion implantation doping of the third-generation semiconductor material SiC.

## As featured in:


See Zongwei Xu, Alexander Hartmaier, Mathias Rommel *et al.*, *J. Mater. Chem. C*, 2021, **9**, 2258.

ROYAL SOCIETY OF CHEMISTRY

rsc.li/materials-c

Registered charity number: 207890

Journal of Materials Chemistry C

ROYAL SOCIETY OF CHEMISTRY

PAPER

View Article Online
View Journal | View Issue



Cite this: J. Mater. Chem. C, 2021, 9, 2258

# MD simulation study on defect evolution and doping efficiency of p-type doping of 3C-SiC by Al ion implantation with subsequent annealing†

Jintong Wu, [a] Zongwei Xu, *[a] Lei Liu, [a] Alexander Hartmaier, *[b] Mathias Rommel, *[c] Kai Nordlund, [d] Tao Wang, [b] Rebecca Janisch [b] and Junlei Zhao [e]

We use molecular dynamics (MD) simulation with numerical characterisation and statistical analysis to study the mechanisms of damage evolution and p-type doping efficiency by aluminum (Al) ion implantation into 3C silicon carbide (SiC) with subsequent annealing. By incorporating the electronic stopping power for implantation, a more accurate description of the atomic-scale mechanisms of damage evolution and distribution in SiC can be obtained. The simulation results show a novel observation that the recrystallization process occurs in the region below the subsurface layer, and develops from amorphous–crystalline interface to the damage center region, which is a new insight into previously published studies. During surface recrystallization, significant compressive stress concentration occurs, and more structural phase transition atoms and dislocations formed at the damage-rich-crystalline interface. Another point of interest is that for low-dose implantation, more implantation-induced defects hamper the doping efficiency. Correspondingly, the correlation between lattice damage and doping efficiency becomes weaker as the implant dose increases under the same annealing conditions. Our simulation also predicts that annealing after high temperature (HT) implantation is more likely to lead to the formation of carbon vacancies ($V_C$).

Received 17th November 2020,
Accepted 9th January 2021

DOI: 10.1039/d0tc05374k

rsc.li/materials-c



## 1. Introduction

As a third-generation semiconductor material, silicon carbide (SiC) is attractive for application in many high-tech areas due to its wide forbidden bandgap, high thermal conductivity, and high electrical breakdown strength.[1] For the fabrication of SiC devices, ion implantation is one key process for almost all kinds of SiC devices due to the low diffusion coefficient of impurities (except boron) in silicon carbide.[2] As for p-type doping, the most commonly used dopants are aluminum (Al) and boron (B). Although some previous studies have investigated B diffusion for p-type doping,[3] a high density of boron-related deep levels[4] is generated, which degrade electrical activation. On the other hand, due to the smaller energy gap to the valence band and a strong tendency to occupy atomic sites in the silicon sublattice,[5,6] and since Al does not appear an abnormal out-diffusion phenomenon as B-doped SiC during annealing,[7] Al is preferred.

Influenced by constraints such as doping amount and impurity atomic distribution, low-resistance p-type SiC preparation is still a difficult problem to be solved,[8] because of ion implantation-induced defects which severely limit carrier lifetime and the effectiveness of doping.[9] Korsunska *et al.*[10] found the recombination centers in 4H-SiC using photoluminescence (PL) spectra. These deep levels caused by compensating impurities were identified as lifetime killers, such as the $Z_{1/2}$ and $EH_{6/7}$ centers.[11–13] Despite several experimental studies on discovering the implantation-induced defects and electrical activation,[14–16] there are several incongruences on the enhancement of electrical activation. For instance, Nipoti *et al.*[14,15,17] indicated that the activation (*i.e.*, implanted ions occupy the targeted lattice sites) of p-type 4H-SiC can be enhanced by increasing the Al-implanted concentration whereas Saks *et al.*[16] claimed the decrease of activation rate is due to the saturation of dopants in SiC at high doping levels. Although a series of

[a] State Key Laboratory of Precision Measuring Technology & Instruments, Laboratory of Micro/Nano Manufacturing Technology, Tianjin University, China. E-mail: zongweixu@tju.edu.cn
[b] Interdisciplinary Centre for Advanced Materials Simulation (ICAMS), Ruhr-University Bochum, Germany. E-mail: alexander.hartmaier@icams.rub.de
[c] Fraunhofer Institute for Integrated Systems and Device Technology IISB, Germany. E-mail: Mathias.Rommel@iisb.fraunhofer.de
[d] Department of Physics, University of Helsinki, Finland
[e] Department of Electrical and Electronic Engineering, Southern University of Science and Technology, Shenzhen, 518055, China

† Electronic supplementary information (ESI) available. See DOI: 10.1039/d0tc05374k

articles based on density functional theory and *ab initio* calculations have conducted related discussions on the origin and properties of fatal defects in SiC,[18–20] while a computational model of p-type doping SiC is completely missing, which limits a fully understanding of the damage evolution mechanism during implantation and annealing. Accordingly, we attempted to answer the following key research questions in this paper:

1. The large amount of energy deposited to the electronic system might lead to the unphysical results, *e.g.* simulations of multiple projectiles. Therefore, how to establish a more realistic model to explore the damage evolution during ion implantation?

2. As for implanted SiC, how the recrystallization happen during annealing? What is the effect of annealing residual damage? How to avoid this?

3. How to connect the doping efficiency in simulations with the electrical activation in experimental study? What are the main factors implicate the doping efficiency, such as dose and implantation temperature: which is the dominant factor under the same annealing conditions?

4. What are the factors affecting the proportion of annealing-induced defects?

In order to answer these questions, we demonstrated the efficiency of substitutional Al-doping of 3C-SiC using molecular dynamics (MD) simulation. Our numerical research is conducted on implantation process and post annealing to clarify the fundamental dynamics of defect recovery. By varying processing conditions such as the doping doses and doping temperature, the optimal p-type doping conditions and the main factors affecting doping conditions were studied. Furthermore, we note that in this context, since the potential function fitting between Al and SiC was based on 3C-SiC,[21] we excluded the idea of using 4H-SiC for the sake of precision of simulation. However, it should be pointed out that the results obtained by studying 3C-SiC can be at least partly applicable for 4H-SiC being most important for today's SiC device fabrication as well because at least to some extent similar defects play an important role for both polytypes. Although the deep level compensation defects mentioned above, such as $Z_{1/2}$ and $EH_{6/7}$ defects, are unique defects of 4H-SiC and 6H-SiC, defects in 3C-SiC that are very similar to these deep energy levels can be found in previous literature. For example, Alfieri[22] reported that the energy position of the deepest level of 3C-SiC labeled K3 ($E_c$ −0.73 eV) is close to that of the $EH_{6/7}$ level in 4H-SiC. And he pointed out that the K3 and $EH_{6/7}$ centers may be related to the same defects through an electron-dose dependent irradiation study. The Z1/Z2 (3C) defect peak observed by Pensl *et al.*[23] in 3C-SiC after implantation is very close to $Z_{1/2}$ peak in 4H-SiC by DLTS spectrum.

Moreover, in the early stages using of SiC as wide bandgap material for the fabrication of advanced power devices, 3C-SiC already attracted a lot of interest due to its physical and electronic characteristics.[24] However, 3C-SiC substrate fabrication and further processing turned out to be more critical due to significantly higher defect densities and defect related issues compared to *e.g.*, 4H-SiC.[25,26] Recently, 3C-SiC gained increasing interest again – strongly due to recent progress in epitaxial growth of 3C-SiC on silicon substrates using dedicated Si surface patterning.[27,28] Thus, today, 3C-SiC is again considered for industrial device fabrication, especially for power MOSFETs due to the rather high channel mobilities[29] and lower interface state densities (Dit) at the $SiO_2$/SiC interface compared to *e.g.*, 4H-SiC,[30] even though very recently, new processing schemes also lead to significant reduction in Dit for 4H-SiC.[31] Therefore, the establishment of Al implanted 3C-SiC with post annealing model to explore the evolution of defects, recrystallization mechanism, and the activation efficiency of doped atoms can still have a certain guiding role on the theoretical level.

## 2. Computational details

### 2.1 Molecular dynamics model and analysis parameters

The simulation work was based on the "Large-scale Atomic/molecular Massively Parallel Simulator" (LAMMPS),[32] and "Open Visualization Tool" (OVITO)[33] was used to visualize and perform data analysis. Furthermore, the statistics over the lattice structure can be gathered by the automated "identify diamond structure" (IDS).[34] Fig. 1 shows the original structure of silicon carbide, where the basic structural unit has a tetrahedral geometry, and it was based on this basic structure to identify the substituted Al atoms. The 3C-SiC supercell composed of a regular tetrahedron structure contains 8 atoms, and the side length of the supercell is 4.348 Å.[35]

The dimensions of our implantation model were 10.87 nm × 10.87 nm × 17.392 nm, including 200 000 atoms. Considering the diffusion effect during implantation, a larger range was adopted in $Z$ direction with non-periodic conditions, while periodic boundary conditions were set in $X$ and $Y$ directions. The SiC workpiece was divided into three zones to describe the actual doping process, *i.e.*, boundary layer, thermostatic layer and Newton layer, as shown in Fig. 2. The operation of atoms in the Newton layer followed Newtonian dynamics (*NVE* ensemble), which directly interacts with the implanted atoms. Temperature of the system increased due to Al continuously bombarding the target, so as to simulate the temperature dissipation in experiment, a few thermostat layer atoms were added at the bottom of the doping region, which were modeled with Berendsen thermostat.[37] The boundary layer was used to fix the position of sample. Moreover, in order to avoid the ion channeling effect,[38] the angle between implantation direction and $Z$ direction was set as 7°. After structural initial equilibration at 293 K, different

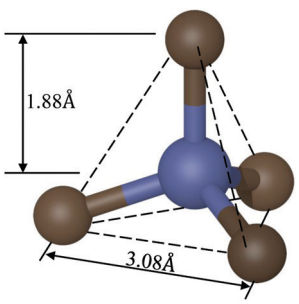


Fig. 1 Essential tetrahedral geometry of SiC.[36] If the central atom is silicon, remaining four represent carbon, and *vice versa*.

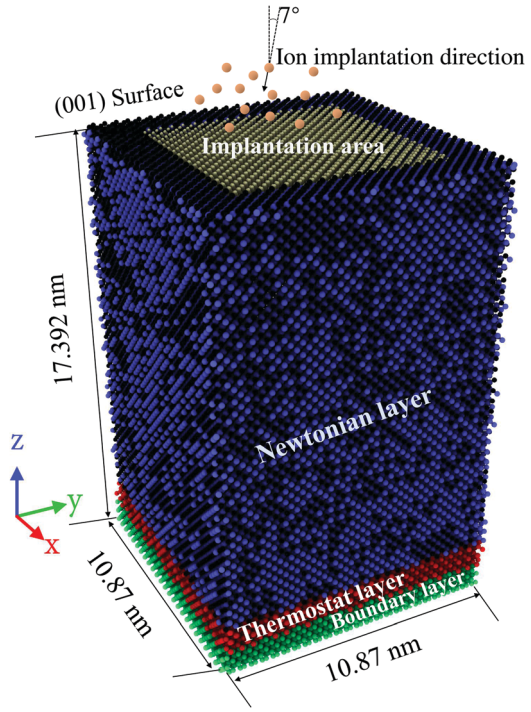


Fig. 2 Ion implantation model of 3C-SiC. The Newtonian layer is colored according to atomic type (silicon atoms shown in blue and carbon atoms shown in black).

numbers of Al ions (corresponding to the doping doses of $1.25 \times 10^{14}$ cm$^{-2}$ to $5 \times 10^{14}$ cm$^{-2}$, corresponding to the same doping area of 8 nm × 8 nm) were simulated bombarding SiC(001) surface with 2 keV energy. Furthermore, a variable-timestep was employed to ensure the simulation accuracy of the rapid motion of particles.

We then studied the recrystallization kinetics and attempted to find efficient Al substitution conditions. Heat control of the annealing system was realized by Nose–Hoover thermostat (*NPT* ensemble). The system was gradually heated to 3300 K (the temperature was selected based on the results of decomposition temperature testing using Tersoff/ZBL potential described in detail in Section 2.3) with 0.5 fs per timestep, and temperature was kept for 2 ns during heating stage. The heating and cooling rate settings were as the same as $2 \times 10^{13}$ K s$^{-1}$. The basic simulation parameters are listed in Table 1.

It might be noted here that the configurations of simulation parameters in MD (such as the implantation energy *i.e.*, 2 and 5 keV) which is one or two orders of magnitude lower than experimental studies (generally in the range from several tens to hundreds of keV). This procedure is however consistent with the inception of such studies,[39–41] and the conventional idea we take in the current simulation is so as to ease off the current limitations of computational time. Moreover, a sufficiently larger size substrate is used to minimize the gap between the experimental and simulation studies. Considering these aspects, it is important to use an appropriate potential function to study the microstructure evolution in implantation and post annealing process.

Normally, the energies and forces of the whole system are described by the potential energy function in MD studies. In this work, Ziegler–Biersack–Littmark (ZBL) repulsive potential was added to accurately correct the short-range interactions between C and Si atoms.[42] The long-range interactions between covalent SiC system was depicted by Tersoff potential,[43] which was splined smoothly to ZBL potential:

$$E = \frac{1}{2}\sum_{i}\sum_{j=1} V_{ij} \quad (1)$$

$$V_{ij} = (1 - f_F(r_{ij}))V_{ij}^{ZBL} + f_F(r_{ij})V_{ij}^{Tersoff} \quad (2)$$

$$f_F(r_{ij}) = \frac{1}{1 + e^{-A_F(r_{ij} - r_c)}} \quad (3)$$

where the $V_{ij}^{Tersoff}$ and $V_{ij}^{ZBL}$ represent the portion of Tersoff and ZBL portion, respectively $r_{ij}$ is the distance between atoms $i$ and $j$. $A_F$ determines the smoothness of the transition between ZBL and Tersoff portion, and $r_c$ is the cutoff for the ZBL function.

The embedded atom method (EAM) potential was used for Al atoms interactions:[44]

$$E = \sum_{i} F_i(\rho_i) + \frac{1}{2}\sum_{i \neq j} \phi_{ij}(R_{ij}) \quad (4)$$

Table 1 Basic parameters of the MD simulation model during ion implantation and post-annealing (as for boundary conditions, p represents periodic boundary conditions, and f represents non-periodic boundary conditions, namely fix boundary conditions)

| Condition | Parameters |
|---|---|
| Work material | Monocrystal 3C-SiC(001) plane |
| Workpiece dimensions | 10.87 nm × 10.87 nm × 17.392 nm |
| Boundary conditions during doping | p p f |
| Incident angle | 7° |
| Doping energy | 2 keV |
| Number of Al ions | 80, 140, 200, 260, 320 |
| Ion doses | $1.25 \times 10^{14}$ cm$^{-2}$, $2.18 \times 10^{14}$ cm$^{-2}$, $3.12 \times 10^{14}$ cm$^{-2}$, $4.06 \times 10^{14}$ cm$^{-2}$, $5 \times 10^{14}$ cm$^{-2}$ |
| Bulk temperature during implantation | 293 K, 873 K, 1273 K, 1973 K |
| Timestep | Adaptive timestep |
| Post implantation annealing temperature | 3300 K |
| Boundary conditions during annealing | p p p |

 

Table 2 Parameters of the Morse potential between aluminum and silicon carbide[45]

| System | Parameters | Morse potential |
|---|---|---|
| Al–C | $D_0$ (eV) | 0.4691 |
| | $\alpha$ (Å$^{-1}$) | 1.738 |
| | $r_0$ (Å) | 2.246 |
| Al–Si | $D_0$ (eV) | 0.4824 |
| | $\alpha$ (Å$^{-1}$) | 1.322 |
| | $r_0$ (Å) | 2.92 |

where $F_i(\rho)$ is the energy of embedding atom $i$ into the electron density $\rho$, and $\rho_i$ is the total electron density surrounding atom $i$. $\phi_{ij}(R_{ij})$ is a pair potential interaction.

Dandekar and Shin proposed a Morse potential to describe the interaction between ceramic and metal particles:

$$E_{ij} = D_0\left[e^{-2\alpha(r_{ij}-r_0)} - 2e^{-\alpha(r_{ij}-r_0)}\right] \quad (5)$$

where $r$ represents the distance between the pair particles, $r_0$ represents the equilibrium bond length, $D_0$ and $\alpha$ represent the well depth and the width of the potential, respectively. Relevant parameters for Morse potential are shown in Table 2, and the accuracy has been tested with *ab initio* study by Zhao *et al.*[21,45]

The stress field is one of the basic parameters characterizing the implantation process. The virial stress was used to analysis the force state of atoms:[46]

$$\sigma_{\alpha\beta}(i) = \frac{1}{NV_i}\left(\sum_i m_i v_{i\alpha} v_{i\beta} + \frac{1}{2}\sum_{i\neq j} r_{ij\beta} F_{ij\alpha}\right) \quad (6)$$

It is a second order tensor, where $m_i$ is the mass of atom $i$, $V_i$ reflects a certain volume around the atom. Note that the area $V_i$ should not be too large to prevent the statistical average covering up the details of the stress field. In this study, the calculation box radius for each atom was set to 2 nm. $N$ represents the number of atoms in the region, $m_i$ and $v_{i*}$ are the mass and velocity of the atom, $r_{ij*}$ and $F_{ij*}$ are the relative vector diameter and force component between a pair of particles, respectively. Temperature calculation is similar to the method used in stress analysis according to the formula:

$$T_i = \frac{2}{3N_i K_B}\left(\sum_{i=1}^{N_i} E_k\right) \quad (7)$$

where $E_k$ is the kinetic energy of the system, $K_B$ is the Boltzmann constant, $T_i$ and $N_i$ are the temperature and number of atoms of the $i$th volume element.

### 2.2 Electronic stopping powers for ion implantation process

In the process of high-energy ion implantation, the mechanisms for dissipating energy of an energetic incident ion can be divided into three categories, namely, nuclear stopping corresponding to elastic collisions, electronic stopping corresponding to inelastic collisions, and charge exchange process. Since the charge exchange loss only accounts for a small part of the total energy loss of low-charge ions, it can be ignored.[47] Although for the simulations in this work (*i.e.*, incident particle energies from 350 eV to 5 keV) nuclear stopping dominates for each implanted ion which can be confirmed using the stopping and range of ions in matter (SRIM) code,[48] while the accumulated error due to the neglect of electronic stopping will become larger as the number of ions increases. The purpose of this test is to augment support to the simulation accuracy, and to have a clear understanding of the damage evolution during ion implantation simultaneously.

The energy of the projectile was varied between 350 eV, 2 keV and 5 keV. The model in Fig. 2 corresponds to the implantation energy of 350 eV and 2 keV, and a 14.78 nm × 14.78 nm × 49.56 nm size of material (including 1 054 272 atoms) was built for 5 keV implantation. In order to eliminate the influence of lattice thermal vibration on damage evolution analysis, we adopted single ion implantation and set the temperature to 0 K. The basic parameters such as boundary conditions and ensemble setting were the same as the ones described in Section 2.1 with an adaptive timestep. A command named "fix electron/stopping" provided by LAMMPS can be used to simulate the electronic blocking power of intermediate energy values. The electronic stopping power is calculated by linear interpolation between two nearest points in the electronic stopping table obtained by SRIM-2013. Specifically, the ionization energy was applied by introducing additional friction force to an energetic atom moving with the kinetic energy exceeding a certain threshold (10 eV by default).

Simulations of the ion implantation process with electronic stopping (Elstop) and without electronic stopping (Elstop-off) were compared. Taking 5 keV implantation as an illustration, during the bombardment, the kinetic energy of Al atoms dropped sharply, which caused the potential energy of material atoms (potential energy of material was calculated from the Tersoff potential function described in Section 2.1) raised by leaps and bounds, as shown in Fig. 3. Due to the introduction of implantation energy, a part of the initial energy loss was promptly transferred to electrons. As the kinetic energy was

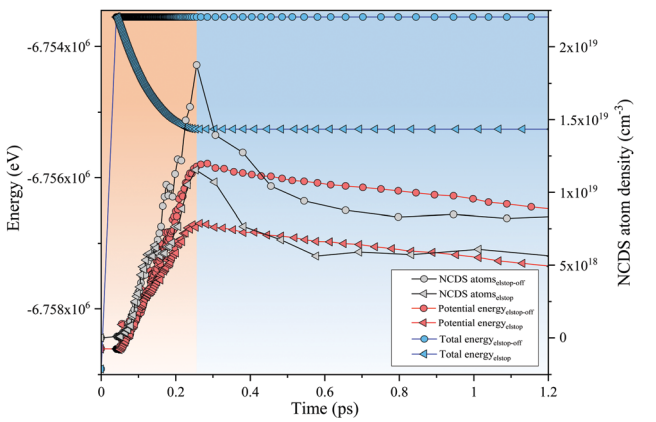


Fig. 3 Variation in the total energy, potential energy and damage atoms counts from Elstop-off and Elstop for 5 keV single-ion implantation. The orange area represents the cascade collision stage, and the blue area represents the damage self-recovery and stability stage. The triangle represents the Elstop implantation and the circle represents the Elstop-off implantation. Due to the use of adaptive timestep, the sampling frequency in collision stage is higher than that in subsequent self-recovery stage.

dissipated, the ionization energy loss rate of the system began to slow down. When the damage of the workpiece reached the maximum, the potential energy of system climbed to the peak value. The ratio of ionization energy lost to recoils revealed three distinct values *i.e.* 32% from 5 keV doping, 17.5% from 2 keV doping and 14.5% from 350 eV doping. In addition, it should be mentioned that we determined the atomic concentration by dividing the number of non-cubic diamond structure atoms (*i.e.*, highly disordered atoms, named NCDS atoms, which were screened out by IDS scheme) atoms by the total volume of material for thermal spike analysis in Section 2.2. As for the subsequent multi-ion implantation, the damaged atom concentration of implanted area was obtained from the ratio of NCDS atoms' count to the volume of the implanted area. Because of the lateral cascade collision effect along $X$ and $Y$ directions during implantation, the area in $X$ and $Y$ directions were chosen as the size of material *i.e.*, 10.87 nm × 10.87 nm. The damage depth is selected as 9 nm (see Fig. S6 and its explanation, ESI†). Using the concentration of crystalline SiC material after initial equilibration (*i.e.*, ~9.72 × $10^{22}$ $cm^{-3}$ in our simulation) as a reference, it can be seen from the concentration of NCDS atoms that ionization (aim at atoms with kinetic energy greater than 10 eV) can weaken cascade collisions within the material, where the stable NCDS atom concentration decreased from ~1.15 × $10^{19}$ $cm^{-3}$ to ~5.72 × $10^{18}$ $cm^{-3}$ for Elstop and from ~1.87 × $10^{19}$ $cm^{-3}$ to ~8.31 × $10^{18}$ $cm^{-3}$ for Elstop-off. The entire process takes about 0.6 ps and 0.8 ps for Elstop and Elstop-off implantation, respectively.

The temperature of heat diffusion was calculated to investigate the fast and slow recovery process. A general exponential function was used to describe the dynamic thermal diffusion:[49]

$$T = T_0 + A_1 e^{-\frac{t}{t_0}} \quad (8)$$

where $T_0$, $A_1$ and $t_0$ are constants. By fitting the curve, it can be calculated that the temperatures of the two systems at the initial time are 2771.7 ± 99.0 K and 2407.8 ± 63.9 K respectively, indicating that the damaged atoms without considering the ionization energy caused a higher local temperature, and $t_0$ represents the rate of temperature drop. When 0 ps < $t_0$ < 1 ps, the smaller $t_0$ means the faster cooling rate. Obviously, it can be observed in Fig. 4 that the cooling rate of Elstop implantation is significantly faster than that of Elstop-off implantation, which is in line with expectations (*i.e.*, considering the loss of energy to electrons, the cooling rate of system will be accelerated).

Furthermore, in order to evaluate the accuracy and validity of MD calculation and in response to the subsequent simulation process, the statistical laws of Elstop and Elstop-off were given by performing 2 keV ion implantation. The doping dose was selected as 5 × $10^{14}$ $cm^{-2}$ with 80 ions (corresponding to the doping area of 4 nm × 4 nm), the damage distribution and Al atom range generated by implantation was compared with SRIM Monte Carlo results. Among them, SiC density was selected as 3.21 g $cm^{-3}$, the incident angle was set to 7°, with 2 keV incident energy and 1 million impacts. Fig. 5 shows the statistics of MD and Monte Carlo results. For the convenience

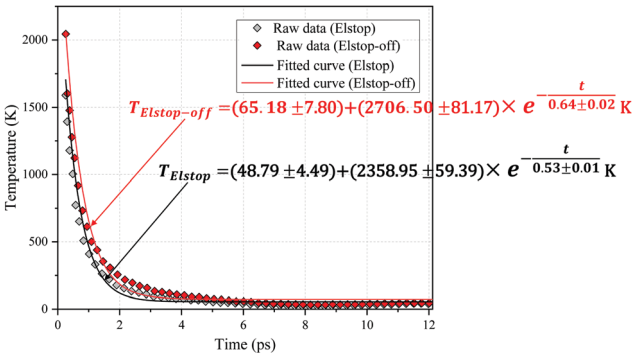


Fig. 4 Average temperature of NCDS atoms and their fitted curve (with confidence bounds >98%) during fast and slow recovery.

of comparison with SRIM results, the atomic density here is obtained according to the ratio of concentration (unit: $cm^{-3}$) to dose (unit: $cm^{-2}$, here the doping dose is 5 × $10^{14}$ $cm^{-2}$). Noted that the calculation principle and the number of implanted ions behind the two methods are quite different, so we mainly focus on the consistency of the distribution. Due to the fact that the energy dissipation of system accelerates when considering the electron stopping powers the penetration depth of the incident particles becomes shallower. Besides, it can be observed from

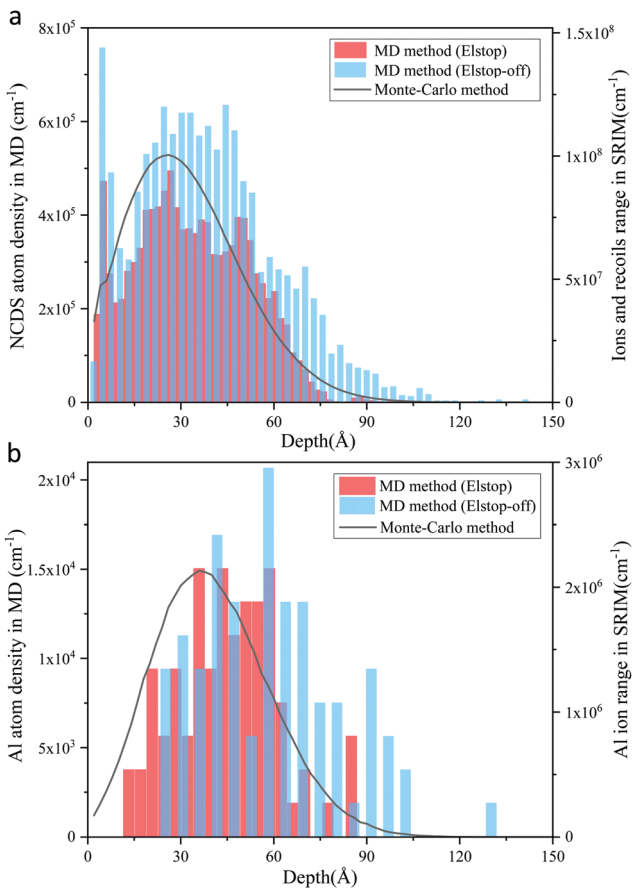


Fig. 5 (a) Damage distributions and (b) Al ions range derived from MD method results and Monte Carlo method (SRIM simulation).

 

Fig. 5 that a better consistency of the distribution of both damaged atoms and projected range in the region with larger penetration depth (greater than 60 Å for damage distribution) exists between Elstop implantation and Monte Carlo method.

### 2.3 Testing of decomposition temperature of SiC by the Tersoff/ZBL potential function

The growth of single crystalline SiC with high purity, complete structure and controllable doping concentration is the basis for fabricating high quality SiC devices. However, it is well known that there is no liquid phase in SiC under vacuum or atmospheric pressure. Since that the annealing temperature is always determined based on the melting point of materials, while as for SiC material, for a more precise definition, here we discuss the decomposition temperature ($T_D$) of SiC, the purpose of this preliminary test was purely to determine the $T_D$ of 3C-SiC under Tersoff/ZBL potential. Compared with the experimental $T_D$ value of 2830 °C for SiC,[50] the according value calculated by the Tersoff potential is often overestimated.[51,52] Therefore, the hysteresis method[53] was carried out to pave the way for the subsequent study of annealing process.

Luo *et al.*[53] explored melting and crystallization for 864 to 10 196 atoms, and found a negligible difference of size effect. In this study, a cubic SiC with a side of 2.6 nm (composed of 1782 atoms) was adopted. Periodic boundary conditions were applied in three directions. The bulk was allowed to follow *NPT* ensembles and was sufficiently equilibrated at 3000 K, with a timestep of 0.5 fs. The ambient temperature was set gradually increased from 3000 K (solid state) to 7000 K (over the DT) with a rate of $2 \times 10^{12}$ K $s^{-1}$. The heating process lasted for 200 million iterations, and then decremental cooling to room temperature (RT) was applied at a constant rate. There will be a saltation in energy at $T_1$ above $T_D$, while during the process of cooling to RT, another sudden saltation in energy will occur at $T_2$ below $T_D$. The calculation of equilibrium $T_D$, can be deduced as:[53]

$$T_D = T_1 + T_2 - \sqrt{T_1 T_2} \quad (9)$$

This can effectively correct the considerable overestimation of $T_D$ when using $T_1$ as the decomposition temperature.[54]

The XRD spectra of 3C-SiC before and after decomposition obtained by virtual X-ray diffraction (XRD)[55] with Cu Kα radiation (1.5418 Å) was given to prove the decomposition process of the crystal. The results are shown in Fig. 6. The peaks correspond to the crystalline SiC at $2\theta$ value of 35.7°, 41.5°, 60.1°, 72.1°, and 75.7°, which is consistent with the typical experimental pattern of beta-SiC powders.[56,57] We have generated additional evidence for the decomposition process by simulating the changes in the coordination number of 3C-SiC before and after decomposition during superheating, which is monitored in Fig. 7. Noted that the coordination number in crystalline SiC is 4, while for the atom that tends to sublimate, this value is often less than 4 due to the appearance of vacancies (that is, due to the dispersion of neighbor atoms). It can be clearly seen that the proportion of Si atoms forming vacancies around is 20% higher than that of C atoms, which means that Si atoms are more likely

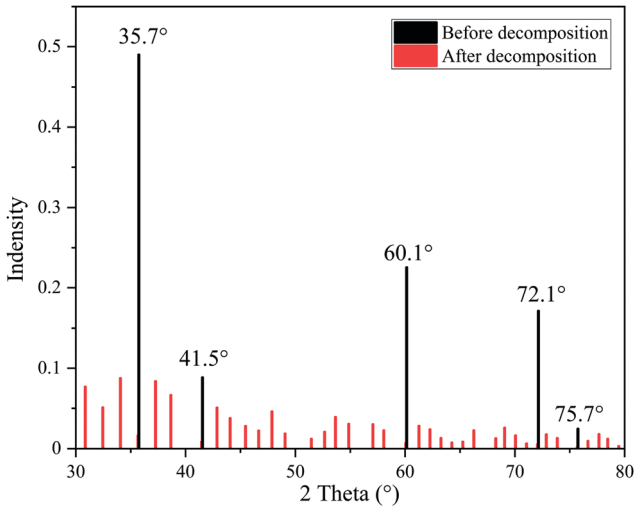


Fig. 6 XRD spectra of 3C-SiC before and after decomposition at the 1st energy transition node temperature $T_1$.

to vaporize than C atoms when the temperature exceeds $T_D$ during superheating. The experimental results show that SiC material begins to sublimate directly above 2000 °C and decomposes into C-rich and Si vapor at high temperature (HT) conditions.[58,59] Moreover, the temperature corresponding to the energy transition of each atom is monitored. As evident from Fig. 8, it is found that $T_1$ and $T_2$ are 5036.0 K and 4425.9 K, respectively. According to eqn (9), it can be concluded that the $T_D$ of SiC calculated based on Tersoff/ZBL potential is about 4740.8 K.

One reason for the higher calculated $T_D$ is that real world materials are never defect-free, and typical defects such as dislocations and impurities tend to lower the melting temperature.[60] It is important to note that an inevitable extrinsic defect in real world is the free surface, and several studies have shown that, the phase-transition temperature can be depressed or the solid can be superheated when the surface conditions are

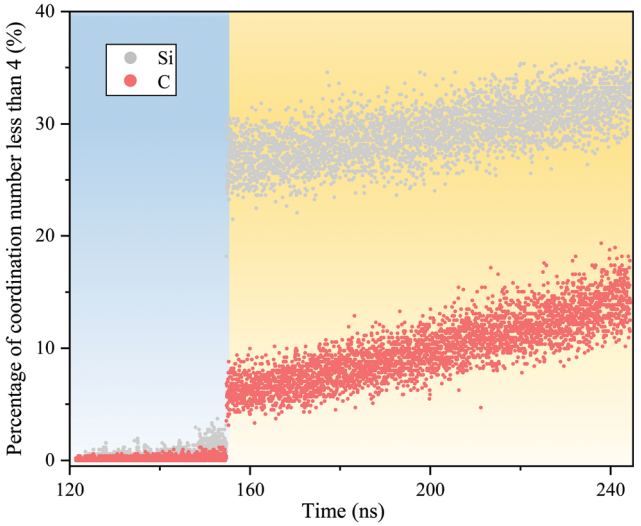


Fig. 7 The variation of atomic coordination number less than 4 in 3C-SiC, before and after decomposition during superheating process.

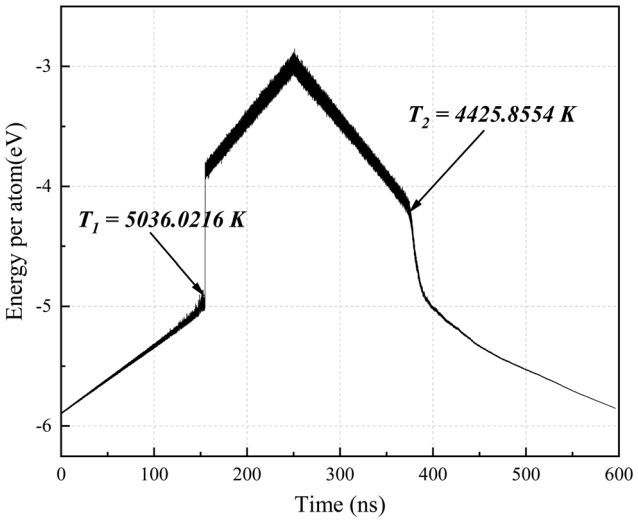


Fig. 8 Temperature hysteresis in energy per atom upon superheating and decremental cooling in isothermal–isobaric ensembles.

modified.[61–64] Some research results have shown that, a perfect crystal without a surface can be superheated substantially above its thermodynamic melting point.[65,66] Actually, HT situation can cause the surface roughness due to the Si desorption from SiC surface in experimental study, or the migration of surface atoms during HT annealing process.[67] The similar results in our simulation are shown in Section 3. The previous experimental work by Nipoti *et al.*[68,69] showed that the annealing temperature range could be selected at 1600–2100 °C, which is about 1000–1500 K lower than $T_D$. Here we take 3300 K as the annealing temperature (provided as ESI† for the choice of HT implantation and annealing temperature in detail). Tersoff potential function modified by ZBL provides a good equilibrium property and can describe the phase transition of materials accurately. In addition, the threshold energy of SiC atom calculated by Tersoff potential function is basically consistent with the experimental results.[70] The accuracy of the calculation of threshold energy is one of the key conditions for the accuracy of calculation in the process of cascade collision during implantation. Moreover, Lampin[52] confirmed that the recrystallization rate calculated by Tersoff potential during recrystallization has a linear relationship with the experimental data and hence it is the obvious choice for performing the implantation and annealing simulations.

### 2.4 Effective method to identify substituted Al atoms

This section focused on the statistical substitution of Si sites by Al doping atoms. The recognition of substitutional atoms or interstitials in OVITO is usually realized by the so-called "Wigner Seitz defect analysis" (WS analysis). This method compares the number of atoms in the same Wigner–Seitz cell in the defect-free reference lattice and with the numbers for subsequent simulations. If there is more than one atom in the in-situ Wigner–Seitz cell, the position is marked as an interstitial.[71] Therefore, when the lattice's fluctuations is not large compared to the initial structure during simulation, the WS method can accurately identify point defects. However, noted that as for implantation process, the evolution process of NCDS atoms identified by IDS and interstitials obtained by WS analysis are shown in Fig. 9. When the first ion bombards the sample, the volume per atom fluctuates greatly, which makes the concentration of interstitials even more than that of subsequent ion implantations with a value of almost $2.1 \times 10^{22}$ $cm^{-3}$, which shows the distinct calculation deviation by WS method. Although relaxation results in a rapid interstitials' reduction, such a large fluctuation will affect our statistical overview of the whole doping process. Therefore, it is unreasonable to use the WS analysis as a basis to judge the existence of interstitials in heating-related simulation, *i.e.*, the WS method is not perfectly suitable for ion implantation and high temperature (HT) annealing process. IDS method calculates the local crystal structure, which is much suitable for the NCDS defect calculation, as shown in Fig. 9. (The details' comparison of IDS and WS analysis during HT dynamic simulations was shown in ESI† for a more intuitive instructions.)

Accordingly, local structure capture combined with IDS was used to identify interstitials and vacancies. Echoing with Fig. 1, an interstitial was determined if there is an extra atom sitting around a cubic diamond structure (CDS) atom within a radius of 2.1 Å. The cutoff value of 2.1 Å was determined empirically by conducting the different radius and finding the range of values which give no significant difference in simulation results. Based on this, we judged bond-creation through the change of distance. When the atom pair is sufficiently far away, it means the bond breaks. The above stipulation is reasonable due to the covalent interaction between SiC atoms without long-range Coulomb force.

Basically, the electrical activation is referred to as: implanted ions will occupy the targeted lattice sites at the end. Hence, we consider the Al atoms that replace the Si lattice position as the Al atoms which contribute to effective doping. As shown in Fig. 10, the first nearest neighbor atom should be four CDS C atoms if the CDS Al atom is regarded as the central atom following this definition. It should be mentioned that the actual simulation results (will be discussed in Section 3) showed that, more Al atoms were recognized as the 2nd

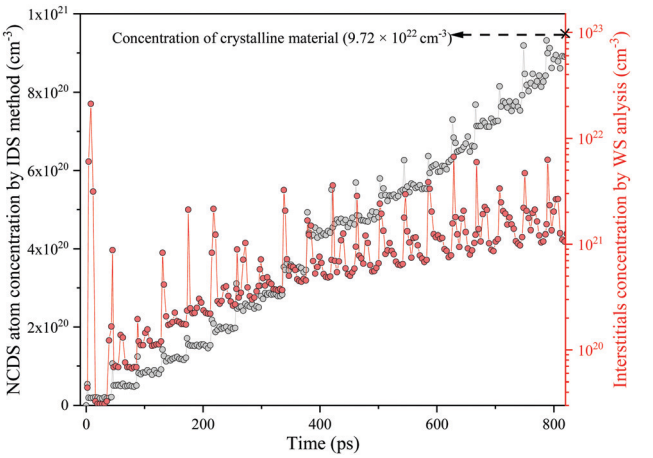


Fig. 9 The concentration of interstitials identified by WS analysis during implantation is compared with NCDS atom concentration obtained from IDS method.

 

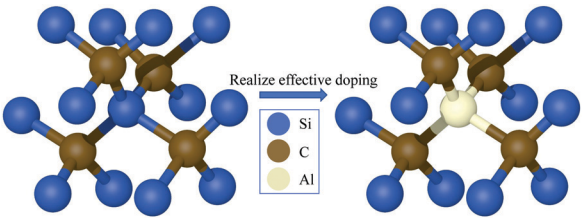


Fig. 10 Schematic diagram of substitution process of Al atom for effective doping.

neighbors of CDS after annealing, which means that the substituted Al atoms lost one or more of their 1st neighbors (C atoms). In particular, the configuration of a substitutional Al on a Si site with an adjacent $V_C$ (namely, $Al_{Si}V_C$ center) was characterized by Wang *et al.*[91] The theoretical results illustrate that the donor features (which is in contrast to the acceptor role of substitutional Al, *i.e.*, $Al_{Si}$) of $Al_{Si}V_C$ may cause a low hole concentration and electrical activation in Al-doped 3C-SiC.[91] Furthermore, the first-principles calculation was used to calculate the band structure of substitutional Al with one carbon divacancy around it ($Al_{Si}$-di$V_C$). The calculation results show the defect levels of $Al_{Si}$-di$V_C$ are below the conduction band minimum (CBM), which reflects the same donor roles as $Al_{Si}V_C$ configuration (see ESI† for the detailed discussion of DFT calculation). Accordingly, to supplement the above theoretical findings and compare with MD results, we considered to classify the "doping efficiency" into "perfect substitution" and "general substitution". Doping efficiency of perfect substitution is defined as:

$$\eta_{\text{Perfect}} = \left(\frac{\text{CDS}_{\text{Al}}}{\text{Total}_{\text{Al}}}\right) \times 100\% \quad (10)$$

and the case of general substitution is defined as:

$$\eta_{\text{General}} = \left(\frac{\text{C1}_{\text{Al}} + \text{C2}_{\text{Al}} + \text{CDS}_{\text{Al}}}{\text{Total}_{\text{Al}}}\right) \times 100\% \quad (11)$$

where $C1_{Al}$ and $C2_{Al}$ are the 1st neighbor CDS Al and the 2nd neighbor CDS Al, respectively. $CDS_{Al}$ reflects CDS Al without the loss of C atoms, and $Total_{Al}$ refers to the total number of doped Al atoms. A more detailed discussion of doping efficiency in this simulation will be given in Section 3.3.

# 3. Results and discussions

## 3.1 Implantation-induced damage

Amorphous atoms can be regarded as NCDS atoms caused by a displacement cascade, which caused the quality of the surrounding lattice structure to deteriorate. Fig. 11 shows the amorphization process during implantation at 293 K. The vertical distribution and area of damage are given by (1 1 0) side central section. In conjunction with Fig. 11, the damage evolution with different ion doses is shown in Fig. 12. Since the ions are implanted one by one until the highest dose (*i.e.* $5 \times 10^{14}$ cm$^{-2}$), the damage evolution can be obtained under a continuous dose. An interesting phenomenon noticeable from Fig. 12 is the curve of NCDS carbon *versus* dose being approximately linear for the whole process, while the difference of the two curves (*i.e.*, NCDS carbon *vs.* dose and NCDS silicon vs dose, respectively) seems to "saturate: when reaching about $3.12 \times 10^{14}$ cm$^{-2}$. As the amorphized layer becomes more and more uniform, we speculate that when the dose continues to further increase, the concentration of damaged atoms of C and Si sublattice eventually becomes saturated. Zhang *et al.* conducted damage accumulation in 4H-SiC, found a sigmoidal dependence on dose.[72] In general, the displacement of C atoms caused by collision cascades is more obvious than that of Si atoms, with threshold displacement energy of 20 and 35 eV, respectively.[73] The saturation of relative Si disorder means a more serious damage caused by cascade bombardment, which would affect the repair effect of subsequent annealing.

To investigate structural changes of the workpiece during implantation, radial distribution function $g(r)$ (RDF) at elevated

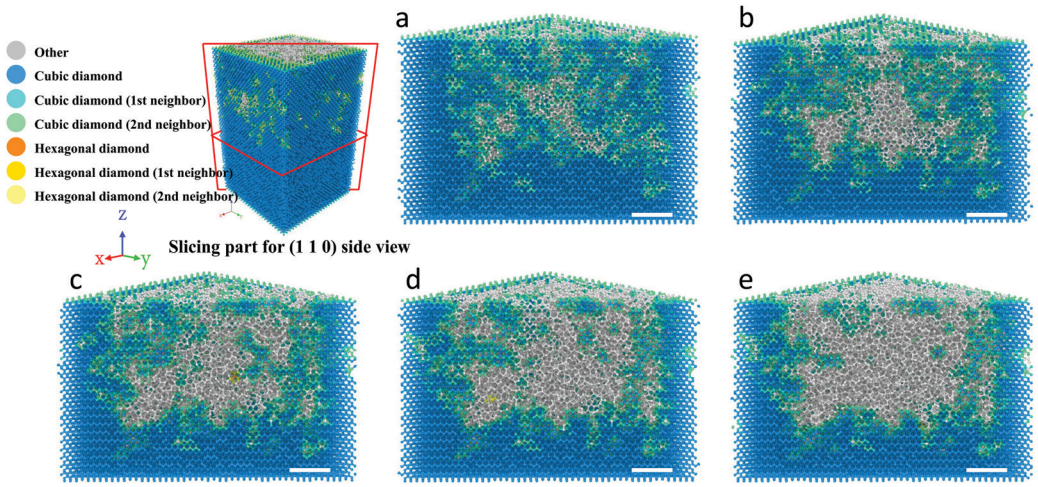


Fig. 11 Snapshots at various stages showing amorphization activity of 3C-SiC during ion energy deposition at 293 K with increasing dose, *i.e.* (a) $1.25 \times 10^{14}$ cm$^{-2}$, (b) $2.18 \times 10^{14}$ cm$^{-2}$, (c) $3.12 \times 10^{14}$ cm$^{-2}$, (d) $4.06 \times 10^{14}$ cm$^{-2}$, (e) $5 \times 10^{14}$ cm$^{-2}$, respectively. Scale bars, 2 nm. Atoms are colored by IDS method.

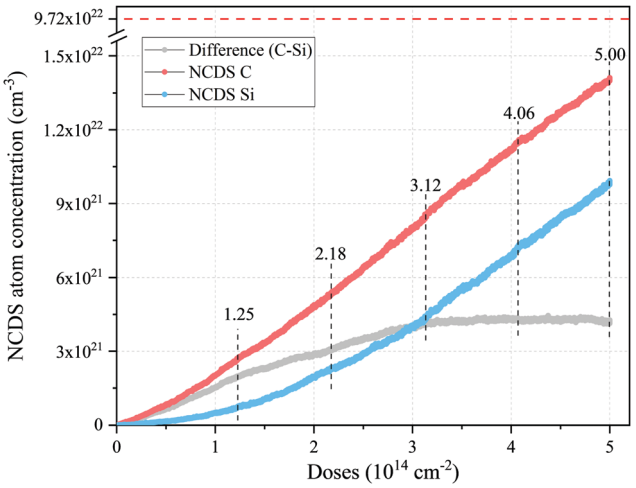


Fig. 12 Relative disorder of implanted area for 3C-SiC irradiated with Al ions at 293 K with doses up to 5 × $10^{14}$ $cm^{-2}$. The continuous horizontal line shows the atomic concentration of the crystalline material as a reference.

doses was calculated. Based on the doping depths given in Fig. 5a (implant dose: 4.06 × $10^{14}$ $cm^{-2}$), we selected a rectangular region with a depth of 5 nm and a 8 nm × 8 nm implanted region for RDF. As seen in Fig. 13, the first peak represents the bonding strength between the nearest neighbor atoms. The deep trough between the first and second peak indicates that the atoms are connected in the form of covalent bonds, and the first peak corresponds to equilibrium bond lengths of 1.875 Å between C–Si in a basic tetrahedral structure, which also proved the rationality of our choice of 2.1 Å as the cutoff to determine the interstitials. Evidently, with increasing dose, the peak intensity keeps decreasing, indicated that implantation has caused a decrease in the bonding strength between atoms, and the rise of troughs indicated the gradual destruction of covalent bonds. In addition, the formation of the

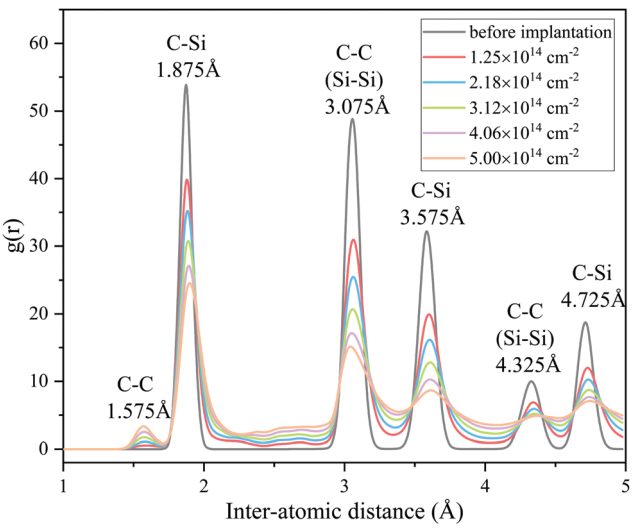


Fig. 13 Radial distribution function of the Al-doped silicon carbide at incremental doses.

C–C bond was confirmed to be due to the embryonic peak at inter-atomic distance of 1.575 Å, which was growing up with the increase of doses. Chavoshi *et al.*[33] reported the formation of C–C bond in 3C-SiC during nanometric cutting, and the equilibrium bond length they measured was at 1.45 Å. The C–C peak reflected the appearance of C interstitials in the basic tetrahedral structure.

### 3.2 Structural evolution during annealing recrystallization

Fig. 14 shows the recrystallization process under different doping doses (2.35 ns, 3300 K HT annealing). It can be seen that the residual damage area remained below the subsurface of the lattice for doses not exceeding 4.06 × $10^{14}$ $cm^{-2}$ (Fig. 14a–d) after annealing. However, the free surface failed to form a closed crystal plane under the same annealing conditions when subsurface damage was homogenized in the highest dose (Fig. 14e). We choose one of the representative implantation dose models, that is, implantation at the dose of 4.06 × $10^{14}$ $cm^{-2}$ model that just formed a closed crystal surface after annealing, to clarify the mechanism of lattice recrystallization.

Fig. 15 and 16 reveal the annealing process details after implantation at the dose of 4.06 × $10^{14}$ $cm^{-2}$. As for angle distribution, Si–C–Si represents the angle between C atom and surrounding Si atoms, and *vice versa*. As shown in Fig. 16, both Si-centered and C-centered structures have a more concentrated angular distribution after annealing, which is manifested in enhancement of peak intensity and narrowing of width. The damage peak between 60° and 80° represents a degree of disorder of C atoms around Si, which also weakened after annealing. The increase of bond angular strength of perfect tetrahedral arrangement (*i.e.*, 109.47°) also implies an increase of crystalline concentrations in the implantation region during annealing process. The region where concentrated residual damage remains inside the workpiece, is about 2–3 nm below the surface, as seen in Fig. 15. The repair of crystal lattice always starts from the interface of the amorphous–crystalline region, *i.e.*, recrystallization always wrapped around subsurface and bottom boundary then grew toward damage center, which is a novel insight compared to the results observed by Xiao *et al.*[74] One reason is that the cascade collision is often occur inside lattice, which causes displaced defects are mainly distributed at a certain depth below the surface.

Another phenomenon should be concerned is that implantation-induced defects often segregate inside the implanted region during annealing, and may introduce additional stress, leading to the formation of new dislocations or stacking faults.[67] Hence, we then illustrated the distribution of structural transition atoms during annealing at 0.5 ns with a dose of 5 × $10^{14}$ $cm^{-2}$ using the construct surface mesh algorithm,[75] as shown in Fig. 17. Only the interface area surrounded by NCDS atoms and diamond configuration atoms undergoing structural phase transition is retained. It can be seen intuitively that some atoms in the interface region have transformed from zinc blende structure to a hexagonal diamond structure. In fact, five different dose annealing models all had phase-transition at damage interface region. Moreover, the

 

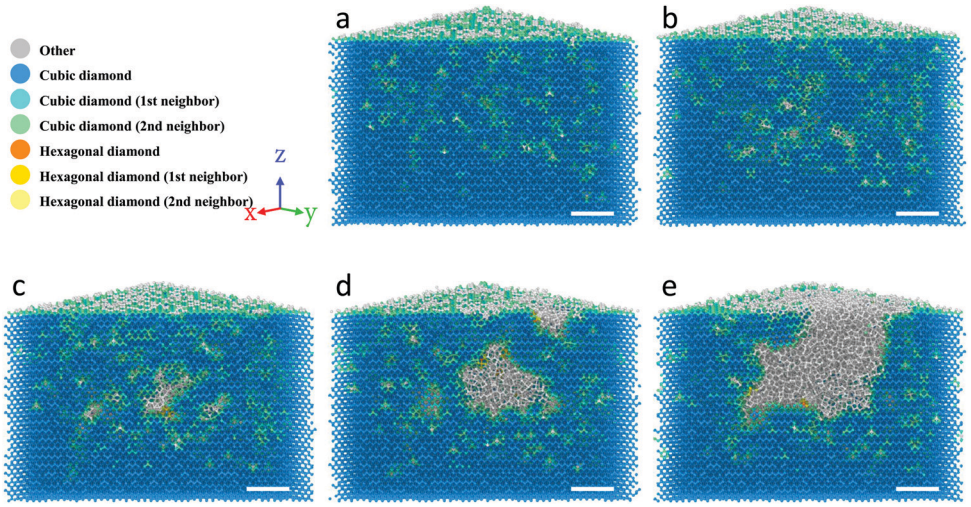


Fig. 14 The cross-sectional (1 1 0) side view of the final lattice structure for different doping doses after 2.35 ns uniform-condition annealing: (a) $1.25 \times 10^{14}$ cm$^{-2}$, (b) $2.18 \times 10^{14}$ cm$^{-2}$, (c) $3.12 \times 10^{14}$ cm$^{-2}$, (d) $4.06 \times 10^{14}$ cm$^{-2}$, (e) $5 \times 10^{14}$ cm$^{-2}$, respectively. Scale bars, 2 nm.

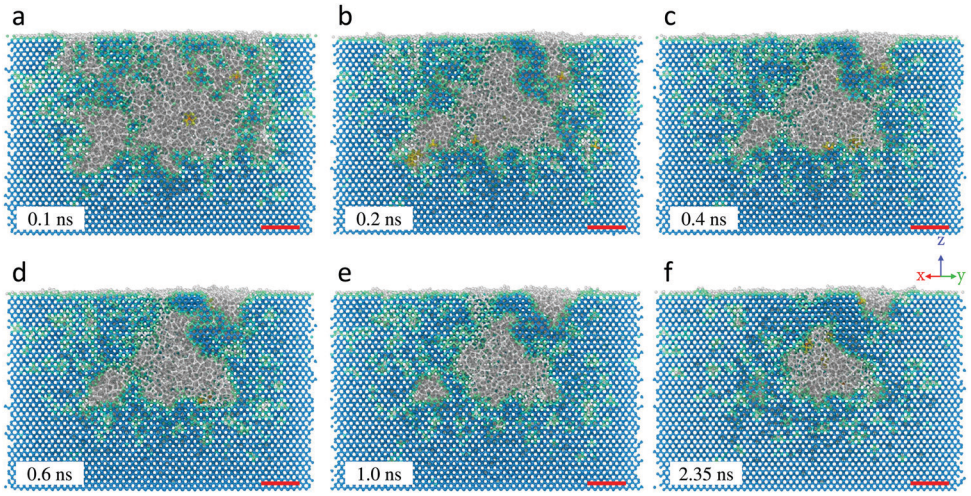


Fig. 15 (1 1 0) side perspective view of recrystallization process under 3300 K, with a doping dose of $4.06 \times 10^{14}$ cm$^{-2}$. Scale bars, 2 nm.

proportion of phase transition atoms in interface region increased with increasing implantation dose. In addition, using the dislocation extraction algorithm (DXA),[76,77] we found some unnamed dislocations and 1/4 ⟨110⟩ partial dislocations at damage boundary in the annealing models with doses of $4.06 \times 10^{14}$ cm$^{-2}$ and $5 \times 10^{14}$ cm$^{-2}$, and no dislocation was found in the other three doping doses. The appearance of interface dislocations reflects the lattice mismatch caused by high-dose implantation, which is in common with previous experimental studies.[78–80] Furthermore, another important question for manufacturing SiC-based devices is their resistance to radiation damage such as displacement effects.[81] Here the distribution of hydrostatic stress was used to evaluate the displacement effects at different doping doses before and after HT annealing, as shown in Fig. 18. It can be seen from Fig. 18a that the evolution of stress distribution that the damaged area presented a particularly high "squeeze" (represented by negative values) due to the existence of interstitials, *i.e.*, stress concentration in implanted region is mainly caused by displacement NCDS interstitials, while contributions of implanted Al are negligible. The whole of undamaged atoms were subjected to tensile stress. Among them, the structure identified by IDS as CDS neighbors was in the interface area, and the corresponding stress value is near 0 GPa. Noted that the tensile stress on the crystallized part of workpiece was released after annealing and maintained at around 0 GPa, as shown in Fig. 18b.

It is natural to speculate whether there is a relationship between the appearance of structural phase transition atoms and compressive stress. In view of this, we quantified the variation of average compressive stress (absolute value) in implantation-induced damage region and concentration of phase transition atoms with different doses. As is evident from

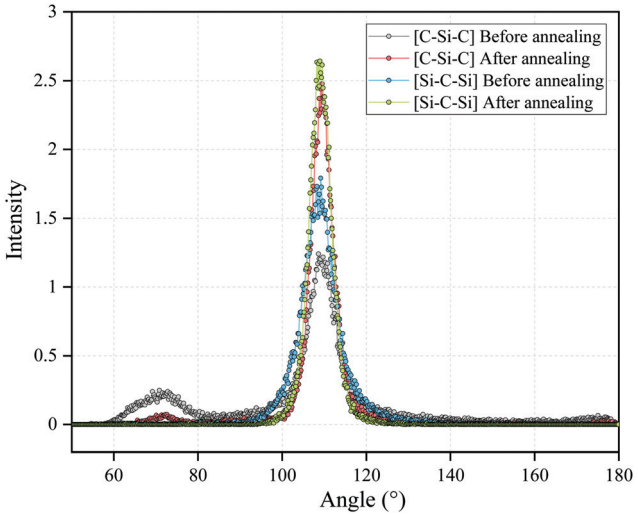


Fig. 16 C–Si–Si and Si–C–Si angle distribution before and after 2.35 ns, 3300 K annealing, with a dose of $4.06 \times 10^{14}$ cm$^{-2}$.

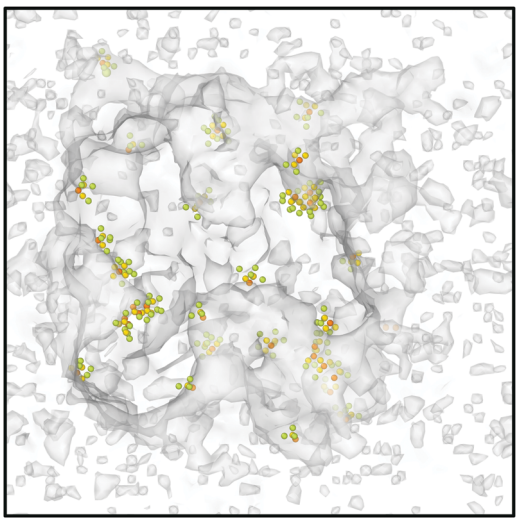

Fig. 17 Distribution of structural transition atoms of (0 0 $\bar{1}$) side view during 3300 K annealing at 0.5 ns with a dose of $5 \times 10^{14}$ cm$^{-2}$ (surface mesh of damage area was constructed using Alpha-shape method, with a probe sphere radius of 1.875 Å). Only hexagonal diamond structure atoms are retained.

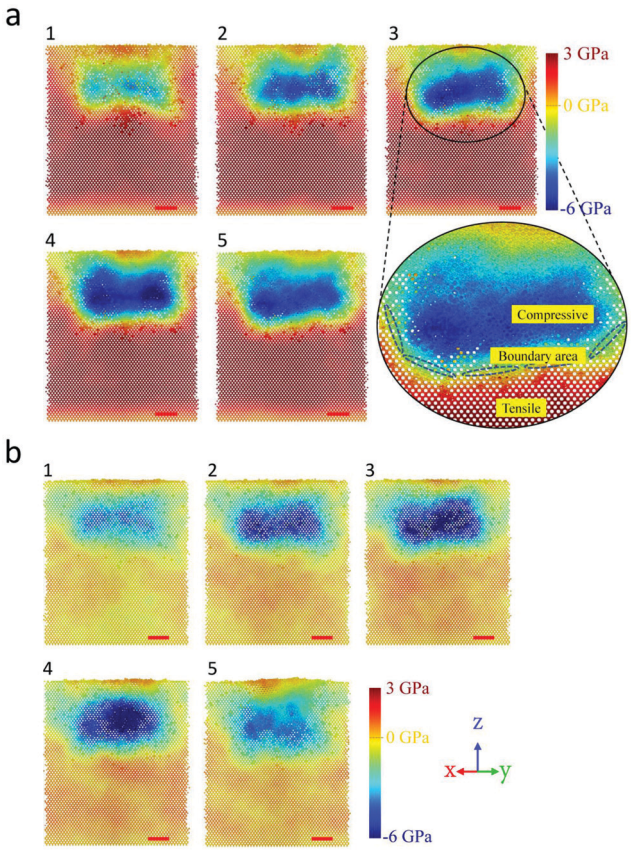


Fig. 18 Hydrostatic stress distribution under different doping doses, (a) before and (b) after 2.35 ns, 3300 K annealing (unit: GPa). The doses corresponding to labels 1–5 are 1.25, 2.18, 3.12, 4.06 and $5 \times 10^{14}$ cm$^{-2}$, respectively. The local details of implantation-induced damage are given under the dose of $3.12 \times 10^{14}$ cm$^{-2}$. Scale bars, 2 nm. Cross-sectional view in (110) direction was adopted.

Fig. 19, the residual damage regions of four doses (except for the implant dose of $5 \times 10^{14}$ cm$^{-2}$) show a higher compressive stress than before annealing due to the formation of the closed crystal surface. On the contrary, the compressive stress is released for the dose of $5 \times 10^{14}$ cm$^{-2}$, *i.e.* no concentrated internal stress is formed because the annealed new born crystals fail to form a closed surface. However, the evolution of phase transition atoms shows an opposite trend: the number of phase change atoms increases dramatically after annealing at high doses (4.06 & $5 \times 10^{14}$ cm$^{-2}$). The evolution of phase transition atoms is more related to the degree of lattice recrystallization rather than the concentration (or release) of stress.

It can be speculated that when the lattice is well-repaired after HT annealing, the increase of phase transition atoms will be effectively suppressed, while additional stress will be introduced at the same time. Therefore, it is necessary to properly extend the annealing time in experiment to decrease the concentration of inner residual defects. A wealth of literature indicates that recrystallization process after annealing may cause crack propagation in the crystal lattice. In experimental research of recent years, Jones[82,83] uncovered an interstitial type dislocation called end-of-range (EOR) damage through TEM micrographs, just below the crystalline/amorphous interface by $Ge^+$-implanted silicon. Ye *et al.*[84] illustrated recrystallization process of carbon irradiated 6H-SiC, and found the volume shrinkage and the anisotropy of the new born crystal during annealing process generated internal stress, which not only produced a large number of dislocation walls but also caused the initiation and propagation of cracks. Hence, the crack propagation or glide of pre-existing basal-plane dislocations can be suppressed by improving the temperature gradient inside the annealing furnace in actual processing.[85] Obviously, the fewer annealing residual defects is more beneficial to reduce crack propagation. Based on the above phenomenon,

 

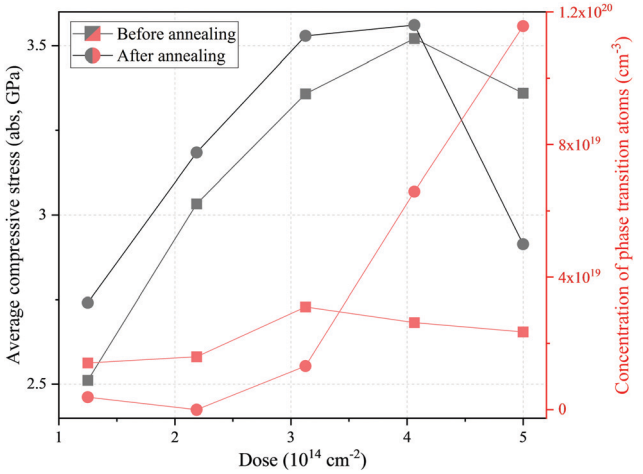


Fig. 19 The variation of average compressive stress (absolute value) in the RT implant-induced damage region and concentration of phase transition atoms with different doping dose before and after 2.35 ns annealing at 3300 K. Red dot chart represents the phase transition atoms, and black dot chart represents the average stress. The two different shape is used to distinguish the state before and after annealing.

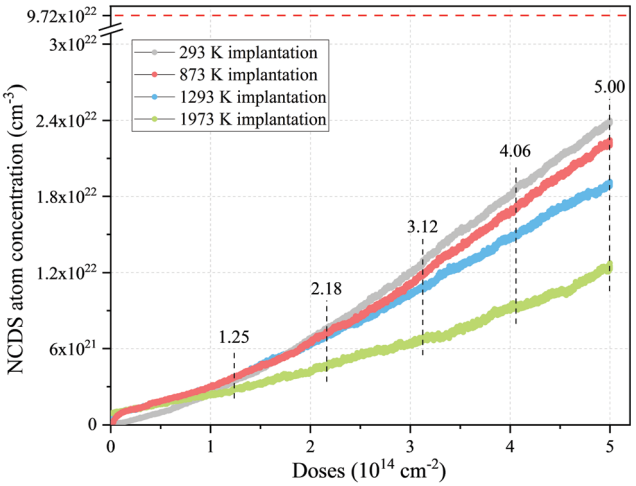


Fig. 20 The NCDS atom concentration of implanted area evolves at different implantation temperatures. Note that as for HT implantation, the NCDS atoms of the undoped workpiece all caused by the vigorous activation of surface atom migration under HT conditions (corresponding to the dose of zero). The continuous horizontal line shows the atomic concentration of the crystalline material as a reference.

here we predict that preventing preferential crystallization of the surface and the formation of residual damage can suppress the additional concentration of internal compressive stress, thereby reducing the occurrence of dislocation slip in actual processing.

### 3.3 Further enhancement of lattice quality and doping efficiency

Previous work has shown that the amorphous state of implanted region is difficult to be annealed out[67] with a high dose implantation. Because of complex polymorphs and low stacking fault energy in SiC, it is very important to maintain the original crystal structure during ion implantation.[7,86,87] Therefore, the evolution of lattice damage and the substitution of Al at HT implantation was explored. The doping temperature was increased to 873 K, 1273 K and 1973 K under the same other conditions, and the workpiece was cooled to RT at the end of subsequent annealing process.

HT implantation causes more damage than that at RT when dose is low, as seen in Fig. 20, due to the appearance of amorphous atoms on the surface when relaxation equilibrium is carried out at HT conditions. The increase of dose aggravated the difference in the concentration of NCDS atoms between HT implantation and RT implantation. From this point of view, HT implantation is more friendly for high dose doping. The additional evidence for the difference of lattice quality after post implantation annealing (implant dose: $5 \times 10^{14}$ cm$^{-2}$) was generated by selected area electron diffraction (SAED) patterns by the computed SAED feature[55] of LAMMPS, as shown in Fig. 21. The value of the parameter $c$ in this algorithm controls the spacing and resolution of reciprocal lattice, and the simulated electron radiation acceleration voltage was selected as 200 kV.[88] We selected the same region as the calculated RDF to characterize the virtual SAED. The diffraction intensity pattern was obtained at the intersection of the reciprocal lattice mesh and the surface of the Ewald sphere with a thickness of 0.01 Å. In terms of repair results of concentrated damage area, the SAED patterns of HT implantation is obviously better than that of RT implantation, *i.e.*, the degree of amorphization reflected by the SAED patterns has a good corresponding relationship with the concentration of NCDS atoms at the highest dose ($5 \times 10^{14}$ cm$^{-2}$) shown in Fig. 20.

In addition, we investigated the doping efficiency at different implantation temperatures, as Fig. 22 shows. On the one hand, echoing with Fig. 20, we considered the degree of lattice damage influencing doping efficiency significantly in low-dose-implanted annealing. For low-dose implanted annealing, such as in the cases of implant dose of $1.25 \times 10^{14}$ cm$^{-2}$, HT implantation is not necessary and may even lead to the decrease of both general and perfect substitution efficiency. Comparing the substitutions of the two cases, it is noted that in addition to the difference in efficiency (25–60% for general substitution, and 2.5–18% for perfect substitution), the trends in these two cases are almost the same, *i.e.*, the substitution yield shows a strong correlation with the dose at both HT and RT implanted-annealing, and high-doses implantation have led to a substantial decrease in the proportion of substituted Al atoms. There is a similar phenomenon in the experiment *e.g.*, Saks *et al.*[16] obtained only 6–35% of Al electrical activation rate at $4.25 \times 10^{15}$ cm$^{-2}$ dose at 650 °C implantation with subsequent annealing at 1700 °C for 30 min. The low percentage of perfect substitutes illustrates that most of the Al atoms occupying Si sites are surrounded by C vacancies. Some theoretical calculation literatures explain the reason for this phenomenon. For instance, Gali *et al.*[89] reported the situation in 4H-SiC obtained by *ab initio* calculation, showed some kind of $V_C$ can be trapped by substitutional Al even after very high temperature annealing. Moreover, first-principles calculation results[90,91] indicate that $Al_{Si}V_C$ shows a lower formation energy than that of either a $V_{Si}$ or a $V_C$ in 3C-SiC. On the other hand, the results in Fig. 22 indicates that

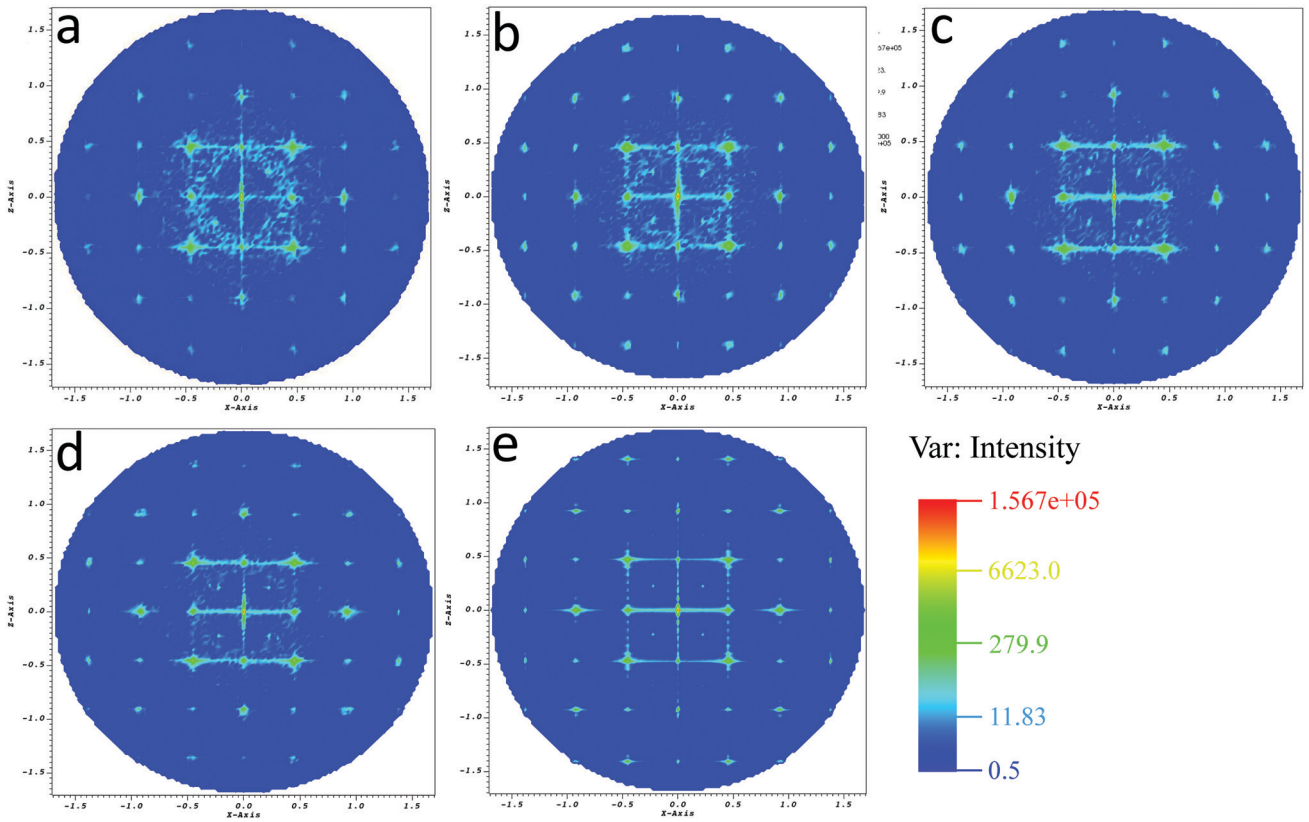


Fig. 21 SAED patterns of SiC aligned with the (010) orientation after post implantation annealing (2.35 ns, 3300 K HT annealing). (a) post RT-implantation annealing, (b) post 873 K implantation annealing, (c) post 1273 K implantation annealing, (d) post 1973 K implantation annealing, with a dose of $5 \times 10^{14}$ cm$^{-2}$ in all cases, and (e) before implantation as a reference.

1273 K implanted-annealing gets the highest general doping efficiency, while 873 K gets the highest perfect doping efficiency in almost all doses (especially at the dose of 2.18 and 3.12 $\times$ $10^{14}$ cm$^{-2}$), and the difference between the doping efficiency obtained from HT and RT implanted-annealing becomes smaller as the dose increases. From perfect substitution situation it can be found that there is no correlation between the existence of $V_C$ around Al and the implantation temperature (*e.g.*, the perfect substitution of 1273 K implantation gets the lowest efficiency under a dose of 4.06 and $5 \times 10^{14}$ cm$^{-2}$ comparing with the other three implantation situations). The two results of perfect substitution and general substitution in Fig. 22 both showed that the overall substitution concentration is gradually increased although the doping efficiency dropped with the ion dose. Comparing with the results of RT implantation, the HT implantation does not obvious improve the doping efficiency. Kimoto's experimental study[67] shows that the situation is significantly changed: the electrical activation of Al ions can be greatly improved under HT conditions when the dose larger than $10^{15}$ cm$^{-2}$, compared with RT implantation. However, this phenomenon was not observed at the dose range in our current simulation (1.25–5 $\times$ $10^{14}$ cm$^{-2}$). It is worth mentioning that from the results of Fig. 20, the ion dose's increase enlarges the difference of NCDS atom concentration between RT and HT implantation. Further MD simulation for the ion dose larger than $10^{15}$ cm$^{-2}$ will be performed in the near future. Therefore, from the above, it can be preliminarily believed that although HT implantation has a significant positive effect on the reduction of lattice damage at high-dose implantation (shown earlier in Fig. 20 and 21), however, the less implantation-induced lattice defects does not mean the higher doping efficiency under the same annealing conditions.

We now transition our focus to investigate the local structural configuration of Al atoms which are not eventually "sit" on the targeted Si sites. Taking 3300 K annealed model (after 1273 K implantation with a dose of $5 \times 10^{14}$ cm$^{-2}$) as an example, atoms within the certain cutoff radius were captured around each Al atom (Fig. S9, ESI†). When the cutoff is reduced to 2.1 Å, lattice structure of the nearest atoms around Al can be clearly obtained. Rectangular box shows the local detail of the residual damage region (which can be clearly distinguished from Fig. S9a and b, ESI†) after HT annealing. It can be noticeably seen that there is almost no crystal structure around Al atoms in the high damage concentration region, but full of disordered interstitial C atoms. Aside from these observations, there are two kinds of Al atoms around the damage concentration region. One is the perfect substituted Al atoms, which presents a tetrahedral supercell structure with four C atoms around it, as shown in the detail drawing of circle box. Another common configuration of Al is as the interstitial configuration, *i.e.*, an impurity Al atom occupies a

 

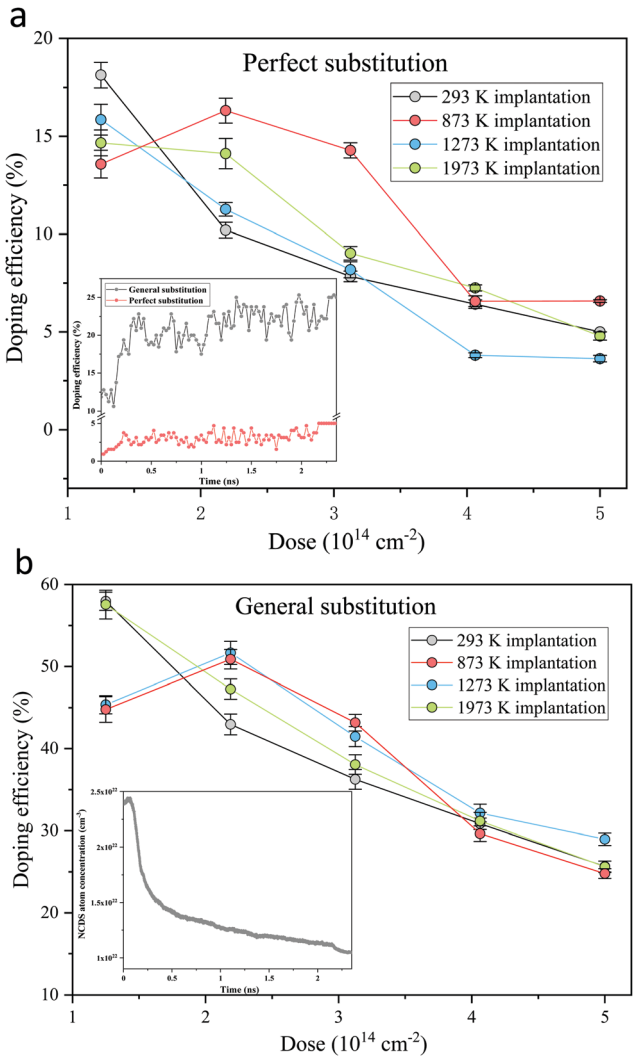


Fig. 22 Implant-dose dependence of doping efficiency (see eqn (1) and (2)) of (a) perfect and (b) general substitution at RT and HT implantation with subsequent 2.35 ns, 3300 K annealing. The inset in (a) shows the evolution of doping efficiency of Al atoms in the same implant conditions (as the highest dose RT implantation produces the most local damage, the certain data is used as an illustration to intuitively reflect the situation that NCDS atom concentration and doping efficiency gradually reach the final saturation state during annealing), the inset in (b) shows the evolution of NCDS atom concentration during the whole annealing process, after 293 K implantation with the dose of $5 \times 10^{14}$ cm$^{-2}$. Due to the smaller sample amount of Al atoms than NCDS atoms, the doping efficiency evolution curve fluctuates more. We average the last 100 000 iterations relaxation after cooling to RT to obtain the final doping efficiency with error bars.

tetrahedral interstitial site (form bonds with the surrounding four C atoms, namely $Al_{TC}$), as shown in the oval box (different directions of the same configuration). However, there are no $Al_{TSi}$ appear in all case. In order to investigate the reason for the common existence of such interstitial Al structures in 3C-SiC, the formation energy ($\Delta E$) was roughly defined (since the limitation of characterize chemical potentials and electrons in MD) according to the following formula:

$$\Delta E = E_{defect} - \frac{N_{defect}}{N_0} \times E_{perfect} \quad (12)$$

Table 3 Formation energies of some typical defective structure shown in MD simulation

| Structure | MD estimation results (eV) | DFT calculation results (eV)[90] |
|---|---|---|
| $Al_{Si}$ | 2.53 | 1.36–1.87 |
| $Al_{TC}$ | 6.29 | 6.12 |
| $Al_{TSi}$ | 8.56 | 8.26 |

where the $E_{defect}$ and $E_{perfect}$ are the total energies of defective (containing defects) and perfect 3C-SiC after energy minimization. The $N_{defect}$ and $N_0$ are the number of atoms in defective and perfect systems (perfect 3C-SiC supercell containing 8000 atoms, with periodic boundary conditions in three directions). The calculation results are shown in Table 3. Combining with the configuration shown in Fig. S9 (ESI†), it can be seen that, although the $\Delta E$ of $Al_{TC}$ is higher than $Al_{Si}$, it is difficult to anneal out due to the stable tetrahedral structure with the surrounding four C atoms, which seriously affects the doping efficiency.

Another point of interest is the introduction of defects at HT conditions. The difference from previous research is that, Kimoto *et al.*[92] were focused on defects induced by annealing temperature, while the main purpose of this part of our simulation is to explore whether the implantation temperature has a significant effect on the annealing-induced defects under the same annealing conditions (see ESI† on how to determine the annealing-induced defects). The percentage of C-related annealing-induced defects (*i.e.*, the carbon interstitials counted by the cutoff radius 2.1 Å, which would be assigned as "other" structure type by IDS scheme) is shown in Fig. 23. Both for RT and HT implantation, a trend of decreasing annealing-induced damaged C with dose shown in Fig. 23 indicates that, the more defects in the lattice, the less defects formed by annealing, which is one of another reasons why HT implantation is usually more beneficial to high-dose conditions. The annealing-induced

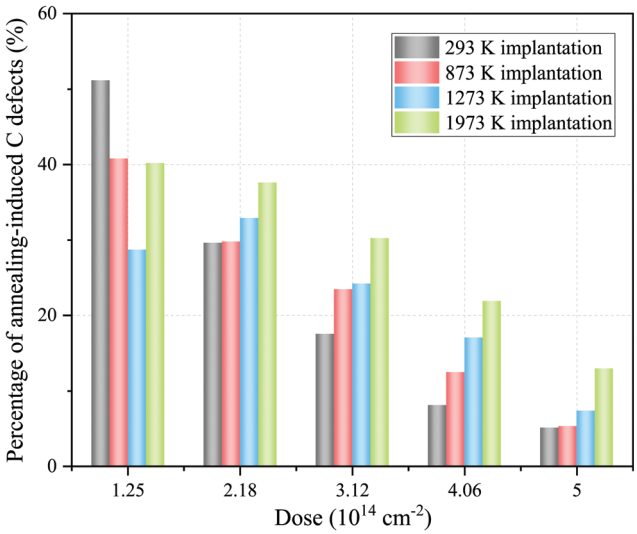


Fig. 23 The percentage of annealing-induced C defects at RT and HT implantation with different doping doses.

defects were always higher for HT implantation than that for RT implantation except for the lowest doping dose. Previous study[67] indicated that HT process such as annealing can easily cause the formation of high-density deep levels, which reduces the carrier lifetime, and these major deep levels produced by ion implantation originate from intrinsic defects. Furthermore, a regular phenomenon shown in Fig. 23 is that HT-implanted annealing will increase the proportion of defects such as $V_C$ *i.e.*, the higher the implantation temperature, the higher proportion of defects introduced by equal condition annealing. This is one of the reasons why the implantation temperature should not be too high in the experiment.

# 4. Conclusion

Although there are abundant literatures on p-type doping process of the third-generation semiconductor material SiC, research on the build of atomic-scale theoretical model of p-type doping is still in the blank stage, which leads to a lack of understanding on the picosecond and nano scale defect formation under p-type doping. Based on this, we established the implantation and subsequent annealing models of Al doped 3C-SiC by MD simulation, and the process of recrystallization during annealing, the relationship between doping efficiency and implantation temperature with different doping doses was explored. The main conclusions can be drawn as follows:

1. The degree of amorphization can be judged by the increasing rate of damaged Si atoms. When the curves of the damaged Si and C atoms are nearly parallel to each other, it represents the formation of highly concentrated amorphous regions (although the complete amorphization threshold of the damaged region is not reached), such an existence of residual defects after annealing will seriously restrict the fabrication quality of SiC devices. In the damage region formed by implantation, the compressive stress is concentrated due to the concentration of a large number of interstitial particles, and the atoms in non-damaged region are subjected to tensile stress.

2. Annealing of different doping doses gives us a new understanding of the recrystallization process. Compared with previous reports, the simulation results show that the recrystallization always occurs in the region below the subsurface, and the crystallization process proceeds from the damage interface to the damage center region, always tends to form a closed crystal surface. Under the trend of surface recrystallization, more compressive stress concentration, structural phase-transition atoms and dislocation structures grow in damage interface region. This is one of the reasons why a large number of cracks and dislocation propagation appear in annealed SiC after implantation in pervious experimental studies. Based on this observation in our MD results we predict that preventing preferential crystallization of the surface can suppress the additional concentration of internal compressive stress, thereby reducing the occurrence of phase transition structures and dislocation slip in actual processing.

3. The advantages and disadvantages of HT implantation compared with RT implantation were explored. With the increase of dose, the doping efficiency of RT implantation decreased step by step (from $\sim$60% to $\sim$25%), and it should be mentioned this holds for a certain annealing process. For low-dose implantation, more implantation-induced defects limit the doping efficiency. Correspondingly, the correlation between lattice damage and doping efficiency becomes weaker as the implant dose increases under the same annealing conditions. Hence, the optimization of annealing conditions for high-dose implantation is worth exploring (this will be expanded in future studies).

4. The proportion of $V_C$ formed by post annealing at HT implantation is always higher than that of RT implantation. This evidences that the implantation temperature should not be too high in the experiment, which also confirms that carrier lifetime killer, *i.e.*, deep level defects, are easier to form at HT conditions.

# Conflicts of interest

There are no conflicts to declare.

# Acknowledgements

The study is supported by the National Natural Science Foundation of China (No. 51575389, 51761135106), 2020 Mobility Programme of the Sino-German Center for Research Promotion (M-0396), the National Key Research and Development Program of China (2016YFB1102203), the State key laboratory of precision measuring technology and instruments (Pilt1705), and the '111' project by the State Administration of Foreign Experts Affairs and the Ministry of Education of China (Grant No. B07014). The computational work was also supported by Center for Computational Science and Engineering at Southern University of Science and Technology. We acknowledge Roberta Nipoti from CNR-IMM of Bologna for the valuable discussions.

# References

1 C. Ulises Gonzalez-Valle, S. Kumar and B. Ramos-Alvarado, Investigation on the Wetting Behavior of 3C-SiC Surface: Theory and Modeling, *J. Phys. Chem. C*, 2018, **122**, 7179–7186.

2 F. J. Campos, N. Mestres, F. Alsina, J. Pascual, E. Morvan, P. Godignon and J. Millán, Confocal micro-Raman scattering and Rutherford backscattering characterization of lattice damage in aluminum implanted 6H–SiC, *Diamond Relat. Mater.*, 1998, **8**, 357–360.

3 Y. Gao, S. I. Soloviev, T. S. Sudarshan and C. C. Tin, Selective doping of 4H-SiC by codiffusion of aluminum and boron, *J. Appl. Phys.*, 2001, **90**, 5647.

4 S. G. Sridhara, L. L. Clemen and R. P. Devaty, *et al.*, Photoluminescence and transport studies of boron in 4H SiC, *J. Appl. Phys.*, 1998, **83**, 7909.

 

5 Y. Song, Z. W. Xu, R. R. Li, H. Wang, Y. X. Fan, M. Rommel, J. Y. Liu, G. V. Astakhov, G. Hlawacek, B. S. Li, J. Xu and F. Z. Fang, Photoluminescence and Raman Spectroscopy Study on Color Centers of Helium Ion Implanted 4H–SiC, *Nanomanuf. Metrol.*, 2020, **3**, 205–217.
6 J. Weiße, M. Hauck, M. Krieger, A. J. Bauer and T. Erlbacher, Aluminum acceptor activation and charge compensation in implanted p-type 4H-SiC, *AIP Adv.*, 2019, **9**, 055308.
7 T. Troffer, M. Schadt, T. Frank, H. Itoh, G. Pensl, J. Heindl, H. P. Strunk and M. Maier, Doping of SiC by implantation of boron and aluminum, *Phys. Status Solidi A*, 1997, **162**, 277–298.
8 Z. W. Xu, Y. Song and M. Rommel, *et al.*, Raman Spectroscopy Characterization of Ion Implanted 4H-SiC and its Annealing Effects, *Mater. Sci. Forum*, 2019, **963**, 424–428.
9 J. Weisse, M. Hauck, T. Sledzaiewski, M. Tschiesche, M. Krieger, A. Bauer, H. Mitlehner, L. Frey and T. Erlbacher, Analysis of Compensation Effects in Aluminum-Implanted 4H-SiC Devices, *Mater. Sci. Forum*, 2018, **924**, 184–187.
10 N. E. Korsunska, I. Tarasov, V. Kushnirenko and S. Ostapenko, High-temperature photoluminescence spectroscopy in p-type SiC, *Semicond. Sci. Technol.*, 2004, **19**, 833–838.
11 P. B. Klein, B. V. Shanabrook, S. W. Huh, A. J. Polyakov, M. Skowronski, J. J. Sumakeris and M. J. O'Loughlin, Lifetime-limiting defects in $n^-$ 4H-SiC epilayers, *Appl. Phys. Lett.*, 2006, **88**, 52110.
12 T. Hiyoshi and T. Kimoto, Reduction of deep levels and improvement of carrier lifetime in n-type 4H-SiC by thermal oxidation, *Appl. Phys. Express*, 2009, **2**, 041101.
13 K. Kawahara, J. Suda and T. Kimoto, Analytical model for reduction of deep levels in SiC by thermal oxidation, *J. Appl. Phys.*, 2012, **111**, 53710.
14 R. Nipoti and H. M. Ayedh, Defects related to electrical doping of 4H-SiC by ion implantation, *Mater. Sci. Semicond. Process.*, 2017, **78**, 13–21.
15 R. Nipoti, Post-implantation annealing of SiC: relevance of the heating rate, *Mater. Sci. Forum*, 2007, **556–557**, 561–566.
16 N. S. Saks, A. V. Suvorov and D. C. Capell, High temperature high-dose implantation of aluminum in 4H-SiC, *Appl. Phys. Lett.*, 2004, **84**, 5195–5197.
17 R. Nipoti and R. Scaburri, Conventional thermal annealing for a more efficient p-type doping of $Al^+$ implanted 4H-SiC, *J. Mater. Res.*, 2013, **28**, 17–22.
18 E. Scalise, L. Barbisan, A. Sarikov, F. Montalenti, L. Miglio and A. Marzegalli, The origin and nature of killer defects in 3C-SiC for power electronic applications by a multiscale atomistic approach, *J. Mater. Chem. C*, 2020, **8**, 8380–8392.
19 A. Gali, T. Hornos, P. Déak, N. T. Son, E. Janźen and W. J. Choyke, Theoretical Investigations of Complexes of p-type Dopants and Carbon Interstitial in SiC: Bistable, Negative-U Defects, *Mater. Sci. Forum*, 2005, **483–485**, 519–522.
20 T. Hornos, A. Gali, N. T. Son and E. Janźen, A theoretical study on aluminium-related defects in SiC, *Mater. Sci. Forum*, 2007, **556–557**, 445–448.
21 H. Y. Zhao, N. X. Chen and Y. Long, Interfacial potentials for Al/SiC(111), *J. Phys.: Condens. Matter*, 2009, **21**, 225002.
22 G. Alfieri and T. Kimoto, Capacitance Spectroscopy Study of Midgap Levels in n-Type SiC Polytypes, *Mater. Sci. Forum*, 2009, **615–617**, 389–392.
23 G. Pensl, T. Frank, M. Krieger, M. Laube, S. Reshanov, F. Schmid and M. Weidner, Implantation-induced defects in silicon carbide, *Physica B*, 2003, **340–342**, 121–127.
24 M. Bhatnagar and B. J. Baliga, Comparison of 6H-SiC, 3C-SiC, and Si for power devices, *IEEE Trans. Electron Devices*, 1993, **40**, 645–655.
25 J. Palmour, H. Kong and R. Davis, Characterization of device parameters in high-temperature metal-oxide-semiconductor field-effect transistors in beta-SiC thin films, *J. Appl. Phys.*, 1988, **64**, 2168.
26 H. Nagasawa, K. Yagi, T. Kawahara, N. Hatta and M. Abe, Hetero-and homo-epitaxial growth of 3C-SiC for MOS-FETs, *Microelectron. Eng.*, 2006, **83**, 185.
27 M. Zimbone, M. Zielinski, C. Bongiorno, C. Calabretta, R. Anzalone, S. Scalese, G. Fisicaro, A. La Magna, F. Mancarella and F. La Via, 3C-SiC growth on inverted silicon pyramids patterned substrate, *Materials*, 2019, **12**, 3407.
28 T. Kreiliger, M. Mauceri, M. Puglisi, F. Mancarella, F. La Via, D. Crippa, W. Kaplan, A. Schöner, A. Marzegalli, L. Miglio and H. von Känel, 3C-SiC epitaxy on deeply patterned Si (111) substrates, *Mater. Sci. Forum*, 2016, **858**, 151–154.
29 F. La Via, A. Severino, R. Anzalone, C. Bongiorno, G. Litrico, M. Mauceri, M. Schoeler, P. Schuh and P. Wellmann, From thin film to bulk 3C-SiC growth: Understanding the mechanism of defects reduction, *Mater. Sci. Semicond. Process.*, 2018, **78**, 57–68.
30 G. Fisicaro, C. Bongiorno, I. Deretzis, F. Giannazzo, F. La Via, F. Roccaforte, M. Zielinski, M. Zimbone and A. L. Magna, Genesis and evolution of extended defects: The role of evolving interface instabilities in cubic SiC, *Appl. Phys. Rev.*, 2020, **7**, 021402.
31 T. Kobayashi, T. Okuda, K. Tachiki, K. Ito, Y. Matsushita and T. Kimoto, Design and formation of SiC (0001)/SiO2 interfaces via Si deposition followed by low-temperature oxidation and high-temperature nitridation, *Appl. Phys. Express*, 2020, **13**, 091003.
32 S. Plimpton, Fast parallel algorithms for short-range molecular dynamics, *J. Comput. Phys.*, 1995, **117**, 1–19.
33 A. Stukowski, Visualization and analysis of atomistic simulation data with OVITO-the open visualization tool, *Model. Numer. Simul. Mater. Sci.*, 2010, **18**, 015012.
34 E. Maras, O. Trushin, A. Stukowski, T. Ala-Nissila and H. Jónsson, Global transition path search for dislocation formation in Ge on Si(001), *Comput. Phys. Commun.*, 2016, **205**, 13–21.
35 A. Taylor and D. S. Laidler, The formation and crystal structure of silicon carbide, Br, *J. Appl. Phys.*, 1950, **1**, 174.
36 S. Z. Chavoshi and X. Luo, Molecular dynamics simulation study of deformation mechanisms in 3C–SiC during nanometric cutting at elevated temperatures, *Mater. Sci. Eng., A*, 2016, **654**, 400–417.

37 H. J. C. Berendsen, J. P. M. Postma, W. F. van Gunsteren, A. DiNola and J. R. Haak, Molecular Dynamics with Coupling to an External Bath, *J. Chem. Phys.*, 1984, **81**, 3684.
38 J. S. Williams, Ion implantation of semiconductors, *Mater. Sci. Eng., A*, 1998, **253**, 8–15.
39 J. Belak, Nanotribology: modelling atoms when surfaces collide, *Energy Tech. Rev.*, 1994, 13–24.
40 S. Goel, S. S. Joshi, G. Abdelal and A. Agrawal, Molecular dynamics simulation of nanoindentation of Fe3C and tetrahedral Fe4C, *Mater. Sci. Eng., A*, 2014, **597**, 331–341.
41 E. H. Åhlgren, A. Markevich and E. Besley, Atomistic Simulations of the Efficiencies of Ge and Pt Ion Implantation into Graphene, *J. Phys. Chem. C*, 2018, **122**, 25700–25708.
42 J. Ziegler, J. Biersack and U. Littmark, *The Stopping and Range of Ions in Solids*, Pergamon, New York, 1985.
43 J. Tersoff, Modeling solid-state chemistry, interatomic potential for multi-component systems, *Phys. Rev. B: Condens. Matter Mater. Phys.*, 1989, **39**, 5566–5568.
44 K. W. Jacobsen, J. K. Norskov and M. J. Puska, Interatomic interactions in the effective-medium theory, *Phys. Rev. B: Condens. Matter Mater. Phys.*, 1987, **35**, 7423–7442.
45 C. R. Dandekar and Y. C. Shin, Molecular dynamics based cohesive zone law for describing Al–SiC interface mechanics, *Composites, Part A*, 2011, **42**, 355–363.
46 W. C. D. Cheong, L. C. Zhang and H. Tanaka, Atomistic structure of monocrystalline silicon in surface nanomodification, *Key Eng. Mater.*, 2001, **196**, 31–42.
47 Z. Tong, X. Q. Jiang, X. C. Luo, Q. S. Bai, Z. W. Xu, L. Blunt and Y. C. Liang, Review on FIB-Induced Damage in Diamond Materials, *Curr. Nanosci.*, 2016, **12**, 685–695.
48 J. F. Ziegler, SRIM-2003, *Nucl. Instrum. Methods Phys. Res., Sect. B*, 2004, **219**, 1027–1036.
49 R. Spohr, *Ion Tracks and Microtechnology, Principles and Applications*, Vieweg, Braunschweig, 1990.
50 W. M. Haynes, *CRC Handbook of Chemistry and Physics*, 97th edn, 2016, pp. 4–84, ISBN 1-4987-5428-7.
51 L. Pastewka, A. Klemenz, P. Gumbsch and M. Moseler, Screened empirical bond-order potentials for Si-C, *Phys. Rev. B: Condens. Matter Mater. Phys.*, 2013, **87**, 205410.
52 E. Lampin and C. Lrzeminski, Molecular dynamics simulations of the solid phase epitaxy of Si: Growth mechanism and orientation effects, *J. Appl. Phys.*, 2009, **106**, 063519.
53 S. N. Luo, A. Strachan and D. C. Swift, Nonequilibrium melting and crystallization of a model Lennard-Jones system, *J. Chem. Phys.*, 2004, **120**, 11640.
54 Y. Qi, T. Çağin, W. L. Johnson and W. A. Goddard III, Melting and crystallization in Ni nanoclusters: The mesoscale regime, *J. Chem. Phys.*, 2001, **115**, 385.
55 S. P. Coleman, D. E. Spearot and L. Capolungo, Virtual diffraction analysis of Ni [0 1 0] symmetric tilt grain boundaries, *Modell. Simul. Mater. Sci. Eng.*, 2013, **21**, 055020.
56 G. Q. Jin and X. Y. Guo, Synthesis and characterization of mesoporous silicon carbide, *Microporous Mesoporous Mater.*, 2003, **60**, 207–212.
57 J. Zheng, H. Chong, L. Wang, S. Chen, W. Yang, G. Wei and F. Gao, A robust SiC nanoarray blue-light photodetector, *J. Mater. Chem. C*, 2020, **8**, 6072.
58 N. G. van der Berga, J. B. Malherbea, A. J. Bothab and E. Friedlanda, Thermal etching of SiC, *Appl. Surf. Sci.*, 2012, **258**, 5561–5566.
59 I. Choi, H. Y. Jeong, H. Shin, G. Kang, M. Byun, H. Kim, A. M. Chitu, J. S. Im, R. S. Ruoff and S. Y. Choi, *et al.*, Laser-induced phase separation of silicon carbide, *Nat. Commun.*, 2016, **7**, 13562.
60 P. Vashishta, R. Kalia, A. Nakano and J. P. Rino, Interaction potential for silicon carbide: A molecular dynamics study of elastic constants and vibrational density of states for crystalline and amorphous silicon carbide, *J. Appl. Phys.*, 2007, **101**, 103515.
61 Ph. Buffat and J.-P. Borel, Size effect on the melting temperature of gold particles, *Phys. Rev. A: At., Mol., Opt. Phys.*, 1976, **13**, 2287.
62 J. B. Boyce and M. Stutzmann, Orientational Ordering and Melting of Molecular H2 in an a-Si Matrix: NMR Studies, *Phys. Rev. Lett.*, 1985, **54**, 562.
63 C. J. Rossouw and S. E. Donnelly, Superheating of small solid-argon bubbles in aluminum, *Phys. Rev. Lett.*, 1985, **55**, 2960.
64 J. Daeges, H. Gleiter and J. H. Perepezko, Superheating of metal crystals, *Phys. Rev. Lett.*, 1986, **119**, 79.
65 J. F. Lutsko, D. Wolf and S. R. Phillpot, Molecular-dynamics study of lattice-defect-nucleated melting in metals using an embedded-atom method potential, *Phys. Rev. B: Condens. Matter Mater. Phys.*, 1989, **40**, 2841.
66 P. M. Agrawal, L. M. Raff and R. Komanduri, Monte Carlo simulations of void-nucleated melting of silicon via modification in the Tersoff potential parameters, *Phys. Rev. B: Condens. Matter Mater. Phys.*, 2005, **72**, 125206.
67 T. Kimoto and J. A. Cooper, *Fundamentals of Silicon Carbide Technology*, Wiley, Singapore, 1st edn, 2014, p. 521.
68 R. Nipoti, A. Nath, M. V. Rao, A. Hallén, A. Carnera and Y. L. Tian, Microwave Annealing of Very High Dose Aluminum-Implanted 4H-SiC, *Appl. Phys. Express*, 2011, **4**, 111301.
69 R. Nipoti, A. Carnera, G. Alfieri and L. Kranz, About the Electrical Activation of $1 \times 10^{20}$ $cm^{-3}$ Ion Implanted Al in 4H-SiC at Annealing Temperatures in the Range 1500–1950 °C, *Mater. Sci. Forum*, 2017, **924**, 333–338.
70 R. Devanathan, Displacement threshold energies in beta-SiC, *J. Nucl. Mater.*, 1998, **253**, 47–52.
71 K. Nordlund, M. Ghaly, R. S. Averback, M. Caturla, T. Diaz de la Rubia and J. Tarus, Defect production in collision cascades in elemental semiconductors and fcc metals, *Phys. Rev. B: Condens. Matter Mater. Phys.*, 1998, **57**, 7556–7570.
72 Y. Zhang, F. Gao, W. Jiang, D. E. McCready and W. J. Weber, Damage accumulation and defect relaxation in 4H-SiC, *Phys. Rev. B: Condens. Matter Mater. Phys.*, 2004, **70**, 125203.
73 Y. Zhang, W. J. Weber, W. Jiang, C. M. Wang and V. Shutthanandan, Effects of implantation temperature on damage accumulation in Al-implanted 4H-SiC, *J. Appl. Phys.*, 2004, **95**, 4012–4018.

 

74 Y. J. Xiao, F. Z. Fang, Z. W. Xu and X. T. Hu, Annealing recovery of nanoscale silicon surface damage caused by Ga focused ion beam, *Appl. Surf. Sci.*, 2015, **343**, 56–69.
75 A. Stukowski, Computational Analysis Methods in Atomistic Modeling of Crystals, *JOM*, 2014, **66**, 399–407.
76 A. Stukowski, V. V. Bulatov and A. Arsenlis, Automated identification and indexing of dislocations in crystal interfaces, *Model. Numer. Simul. Mater. Sci.*, 2012, **20**, 085007.
77 A. Stukowski and K. Albe, Extracting dislocations and non-dislocation crystal defects from atomistic simulation data, *Model. Numer. Simul. Mater. Sci.*, 2010, **18**, 085001.
78 X. Zhang, M. Skowronski, K. X. Liu, R. E. Stahlbush, J. J. Sumakeris, M. J. Paisley and M. J. OfLoughlin, Glide and multiplication of basal plane dislocations during 4H-SiC homoepitaxy, *J. Appl. Phys.*, 2007, **102**, 093520.
79 M. Nagano, H. Tsuchida, T. Suzuki, T. Hatakeyama, J. Senzaki and K. Fukuda, Annealing induced extended defects in as-grown and ion-implanted 4H–SiC epitaxial layers, *J. Appl. Phys.*, 2010, **108**, 013511.
80 X. Zhang, M. Nagano and H. Tsuchida, Correlation between thermal stress and formation of interfacial dislocations during 4H-SiC epitaxy and thermal annealing, *Mater. Sci.*, 2011, **306**, 679–680.
81 J. Chen, P. Jung and H. Ullmaier, Stresses, strains and cracks in a helium-implanted SiC/C composite, *J. Nucl. Mater.*, 2005, **336**, 194–200.
82 K. S. Jones and D. Venables, The effect of implant energy, dose, and dynamic annealing on end-of-range damage in Ge + -implanted silicon, *J. Appl. Phys.*, 1991, **69**, 2931–2937.
83 L. S. Robertson, K. S. Jones, L. M. Rubin and J. Jackson, Annealing kinetics of {3 1 1} defects and dislocation loops in the end-of-range damage region of ion-implanted silicon, *J. Appl. Phys.*, 2000, **87**, 2910–2913.
84 C. Ye, G. Ran, W. Zhou, Q. Shen, Q. J. Feng and J. X. Lin, Recrystallization-induced surface cracks of carbon ions irradiated 6H-SiC after annealing, *Materials*, 2017, **10**, 1231.
85 X. Zhang, T. Miyazawa and H. Tsuchida, Critical conditions of misfit dislocation formation in 4H-SiC epilayers, *Mater. Sci. Forum*, 2012, **313**, 717–720.
86 T. Kimoto, N. Inoue and H. Matsunami, Nitrogen ion implantation into α-SiC epitaxial layers, *Phys. Status Solidi A*, 1997, **162**, 263.
87 J. A. Edmond, R. F. Davis and S. P. Withrow, Structural characterization of ion implanted beta-SiC thin films, *Ceram. Trans.*, 1989, **2**, 479.
88 C. Colliex, in *Electron diffraction International Tables for Crystallography Volume C: Mathematical, Physical, and Chemical Tables*, ed. E. Prince, Kluwer, Norwell, MA, 2004, pp. 259–429.
89 A. Gali, T. Hornos, N. T. Son, E. Janzén and W. J. Choyke, Ab initio supercell calculations on aluminum-related defects in SiC, *Phys. Rev. B: Condens. Matter Mater. Phys.*, 2007, **75**, 045211.
90 N. Matsushima and J. Yamauchi, First-principles X-ray photoelectron spectroscopy binding energy shift calculationfor boron and aluminum defects in 3C-silicon carbide, *Jpn. J. Appl. Phys.*, 2019, **58**, 031001.
91 X. P. Wang, M. W. Zhao, H. H. Xia, S. S. Yan and X. D. Liu, First-principles characterization of an AlSiVC center in cubic silicon carbide, *J. Appl. Phys.*, 2011, **110**, 033711.
92 B. Zippelius, J. Suda and T. Kimoto, High temperature annealing of n-type 4H-SiC: Impact on intrinsic defects and carrier lifetime, *J. Appl. Phys.*, 2012, **111**, 033515.